International Communications in Heat and Mass Transfer 176 (2026) 111420

Contents lists available at ScienceDirect

International Communications in Heat and Mass Transfer

journal homepage: www.elsevier.com/locate/ichmt

Multi-objective optimisation and cyclic performance evaluation of a metal foam-enhanced hybrid battery thermal management system

Alireza Keyhani-Asl [a], Noel Perera [a,*], Jens Lahr [a], Reaz Hasan [a], Parvaneh Zare [b]

[a] *Department of Engineering, School of Architecture, Built Environment, Computing and Engineering, Birmingham City University, Birmingham B4 7XG, UK*
[b] *Queens Building, University of Bristol, University Walk, Bristol BS8 1TR, UK*

ARTICLE INFO

Keywords:
Hybrid battery thermal management system
Copper foam
Energy density
Cyclic performance
Taguchi optimisation

ABSTRACT

High-rate cyclic operation of lithium-ion batteries places strict requirements on thermal management to maintain safety and temperature uniformity. In response, this study presents the design, optimisation, and cyclic performance evaluation of a novel hybrid battery thermal management system (HBTMS) integrating phase change material (PCM), liquid cooling, and copper metal foam as porous fins and layered inserts. A unified architecture is proposed in which copper foam is utilised in two distinct regions, being embedded within the PCM to enhance conduction and integrated within the liquid-cooling channels to intensify forced convection, thereby strengthening the both passive–active heat dissipation mechanisms rather than being confined to a single cooling method. The Taguchi design of experiments (DOE) method was employed to simultaneously optimise the HBTMS with respect to key performance metrics, including the maximum battery surface temperature ($T_{Max,\ Sur}$), maximum temperature difference within the battery module (ΔT_{Max}), performance evaluation criterion (PEC), and energy density (Ed). Numerical simulations employed the enthalpy–porosity method for PCM modelling and the Darcy–Brinkman–Forchheimer (DBF), local thermal equilibrium (LTE), and local thermal non-equilibrium (LTNE) models for porous media. The proposed HBTMS delivered markedly improved thermal performance, maintaining $T_{Max,\ Sur}$ at least 10 K below the safety limit of 323.15 K and limiting ΔT_{Max} under 5 K. A further novelty lies in the comprehensive cyclic evaluation, which explicitly accounts for both discharge and charge phases, demonstrating complete PCM re-solidification and preventing cumulative heat build-up over cycles. Ambient temperature, coolant temperature, and mass flow rate were identified as dominant factors.

1. Introduction

Lithium-ion batteries (LIBs) have become the cornerstone of electric vehicle (EV) and hybrid electric vehicle (HEV) technologies, offering high energy density, long cycle life, and reliable performance. As the transport sector transitions towards low- and zero-emission solutions, driven by environmental regulations and carbon reduction targets, the role of LIBs has grown increasingly critical. However, despite their advantages, LIBs are highly sensitive to temperature variations, which can significantly impact their efficiency, safety, and operational lifespan. The safe and effective operation of LIBs is generally confined to a temperature range of 25 °C to 45 °C [1–3]. Furthermore, to ensure uniform performance and avoid accelerated ageing across battery modules, the temperature variation between cells should not exceed 5 °C [4–7]. These constraints highlight the critical need for advanced thermal management strategies, particularly for LIBs commonly adopted in EV applications.

Hybrid battery thermal management systems (HBTMS), which combine both active and passive cooling techniques, have gained increasing attention as an effective solution for managing the thermal behaviour of LIBs [8]. The incorporation of metal foam into these systems plays a key role in enhancing heat dissipation, as its highly porous and interconnected structure promotes efficient heat transfer through conduction and convection [6]. Additionally, the lightweight nature of metal foams contributes to a reduction in overall system mass, thereby

---

Abbreviations: BTMS, Battery Thermal Management System; CPCM, Composite Phase Change Material; DBF, Darcy–Brinkman–Forchheimer; DOE, Design of Experiments; EV, Electric Vehicle; GCI, Grid Convergence Index; HBTMS, Hybrid Battery Thermal Management System; HDMR, High-Dimensional Model Representation; HEV, Hybrid Electric Vehicle; HPPC, Hybrid Pulse Power Characterization; LIB, Lithium-ion Battery; LTE, Local Thermal Equilibrium; LTNE, Local Thermal Non-Equilibrium; PCM, Phase Change Material; PEC, Performance Evaluation Criteria; PPI, Pores per Inch; S/N, Signal-to-Noise ratio; SOC, State of charge.

* Corresponding author.
E-mail address: noel.perera@bcu.ac.uk (N. Perera).

https://doi.org/10.1016/j.icheatmasstransfer.2026.111420

Nomenclature

Thermal and heat transfer parameters

A	Surface area (m^2)
f_r	Friction factor
h	Convective heat transfer coefficient (W·m^{-2}·K^{-1})
k	Thermal conductivity (W·m^{-1}·K^{-1})
L	Characteristic length (m)
L_f	Liquid fraction
$\overline{Nu}$	Average Nusselt number
ΔP	Pressure drop (Pa)
Q	Total heat generation (W)
q	Volumetric heat generation rate (W·m^{-3})
T	Temperature (K)
$T_{Max,Sur}$	Maximum battery surface temperature (K)
ΔT_{Max}	Maximum temperature difference within battery module (K)
t	Time (s)Electrical and Electrochemical Parameters
C_0	Nominal capacity
E	Open circuit voltage (V)
E_d	Energy density (Wh·kg^{-1})
F	Faraday's constant (96,485C·mol^{-1})
I	Electric current (A)
n	Number of electrons
R_e	Internal resistance (Ω)
ΔS	Entropy change (J·mol^{-1}·K^{-1})
U	Nominal voltage
V	Terminal voltage (V)
$\frac{dE}{dT}$	Entropy coefficient (V·K^{-1})

Greek letters

ε	Porosity
ω	Pore density (PPI)
n_{test}	Total number of test runs

Subscripts

b	Battery
Max	Maximum
gen	Generated
err	Irreversible
rev	Reversible
Sur	Surface
t	Total

improving the energy density of the battery pack [9]. Collectively, prior studies have demonstrated that integrating PCM, liquid cooling, and metal foam can substantially enhance thermal regulation in lithium-ion battery systems. Khaosan et al. [10] investigated an HBTMS for 18,650 LIBs using water, n-eicosane, and copper foam. Their numerical study demonstrated that a combined design of phase change materials (PCM), metal foam, and counterflow minicanal's reduced the maximum battery temperature by up to 11.5 K compared to a passive PCM system while maintaining temperature differences below 5 K, ensuring safe operation and extended PCM lifespan. Moaveni et al. [11] conducted a numerical study on a HBTMS for 18,650 LIBs, integrating water cooling with a nanocomposite PCM composed of RT44HC enhanced by 5% CuO and 5% graphene nanoparticles, along with copper foam. The obtained results showed that the inclusion of copper foam and nanoparticles substantially improved thermal regulation. Compared to pure PCM, the hybrid configuration reduced the maximum cell temperature by 10.6 °C and decreased the temperature difference across cells by 76.5%, indicating enhanced thermal uniformity. Zhao et al. [12] conducted both experimental and numerical analyses on a HBTMS for 18,650 LIBs, incorporating water, paraffin, and copper foam. Their findings demonstrated that increasing the Reynolds number to 112 enhanced the cooling efficiency, resulting in a reduction of the maximum battery temperature by 6 K. However, this improvement was accompanied by an increase in pump power consumption of 59 W, highlighting the trade-off between thermal performance and energy demand. Xie et al. [13] numerically and experimentally investigated an HBTMS that combines liquid immersion cooling with aluminium-encapsulated PCM. The obtained results demonstrated that the hybrid configuration significantly suppressed thermal shock under 5C discharge, reducing the maximum temperature by up to 30.76% compared to a pure immersion baseline and markedly improving temperature uniformity. Furthermore, under low-temperature conditions (−40 °C to 0 °C), the integrated PCM provided 3–7 h of thermal retention depending on ambient temperature, confirming the system's dual-function capability. Li et al. [14] numerically studied an HBTMS integrating CPCM with a wavy microchannel liquid-cooled plate to improve thermal regulation under realistic fast-charging and slow-discharging conditions. Their results showed that the hybrid system effectively reduced peak temperature and maintained temperature differences within approximately 10 °C during continuous charge–discharge cycles, while enhancing thermal homogeneity and low-temperature adaptability. The proposed configuration achieved a 21.69% improvement in effective mass–energy density compared to a conventional liquid-cooled design, albeit with a 24.53% reduction in theoretical mass–energy density due to additional structural mass, highlighting the trade-off between thermal performance and system weight. Wagh and Saha [15] proposed a hybrid PCM–immersion cooling battery thermal management system for 18,650 lithium-ion cells, integrating n-docosane PCM with vertical convective channels and dielectric silicone oil immersion. Their results showed that increasing the number of vertical channels from 8 to 10 reduced the peak cell temperature by 8.9 °C and shortened PCM solidification time by 13.8% at a convective heat transfer coefficient of 200 W/m^2·K. The hybrid configuration limited the maximum cell temperature to 46.3 °C, representing a 29.9 °C reduction compared to a bare cell under natural convection. The study highlighted the trade-off between enhanced convective cooling and structural complexity while demonstrating that the hybrid PCM–immersion approach enables sustained high-rate operation under harsh ambient conditions. Liu et al. [16] found that hybrid systems using water, copper foam, and PCM variants (PCM28HC, PCM35HC, PCM44HC) reduced temperatures by over 30 K compared to natural convection, with a stabilisation point at flow velocities above 0.05 m/s. Although these investigations confirm the thermal benefits of hybrid configurations, the role of metal foam is often confined to a specific region of the system, and comparative evaluation of alternative structural arrangements remains limited. Moreover, most studies assess performance under predefined operating conditions, with limited emphasis on the simultaneous optimisation of interacting geometric and operational parameters.

Studying the cyclic performance of the HBTMSs is essential for evaluating their long-term thermal stability, reliability, and practical viability under realistic operating conditions. Batteries frequently undergo repeated charge and discharge cycles, generating cumulative heat that can compromise safety, efficiency, and lifespan if not properly managed. Therefore, understanding how HBTMS perform across multiple cycles provides critical insights into their ability to mitigate thermal accumulation, preserve cell integrity, and ensure uniform temperature distribution. Extensive experimental and numerical investigations have been conducted to assess the cyclic thermal response of HBTMSs. El Idi et al. [17] investigated a passive system with paraffin and aluminium foam for 18,650 LIBs under repeated 1C charge and discharge cycles, maintaining surface temperatures below 27 °C, achieving full PCM melting, and reducing thermal response time by 35%. Lin et al. [18] proposed a HBTMS for 18,650 LIBs incorporating a CNT@MXene-enhanced composite phase change material (CPCM). The system was evaluated under a fixed 1C charge rate and discharge rates of 2C, 3C, and 4C to assess its cyclic thermal performance. Results demonstrated a significant reduction in maximum battery temperature, from 53.48 °C to 39.09 °C, and a 50% decrease in the temperature rise rate. Notably, the system contributed to extended battery lifespan by 11.83%, 18.92%, and 28.13% at 2C, 3C, and 4C discharge rates, respectively. Liu et al. [19] numerically investigated a lightweight HBTMS for 18,650 LIBs, combining water cooling and CPCM under high ambient temperature and fast cycling. The system was tested under 2C—5C charge and discharge cycles at 40 °C, effectively limiting the maximum temperature to 46.56 °C and temperature difference to 3.06 °C during 5C discharge. Saxena et al. [20] numerically studied a HBTMS for LIB punch cells, combining a PCM-integrated zig-zag cold plate with both continuous and intermittent liquid cooling strategies. The system was evaluated under four realistic driving cycles including Highway Fuel Economy Test (HWFET), Worldwide Harmonized Light Vehicles Test Procedure (WLTP), Urban Dynamometer Driving Schedule (UDDS), and Federal Test Procedure (US-06) and two high-rate discharge and charge cycles (4C—1C and 5C—1C). It improved thermal regulation and reduced maximum temperatures and gradients, particularly under high C-rate cycling. The intermittent cooling strategy significantly reduced energy consumption, up to 83.9% under 4C—1C and 76.7% under 5C—1C, while maintaining effective temperature control. Liu et al. [21] numerically developed and optimised a fin-enhanced HBTMS for 18,650 LIBs operating under high ambient temperatures and extended cycling. The system combined CPCMs, liquid cooling, and solid fin structures to manage heat during continuous charge and discharge at a 2C rate. Under these cyclic conditions at 40 °C, the system maintained the maximum temperature and temperature difference within 42.2 °C and 1.7 °C, respectively. Wang et al. [22] conducted an experimental and numerical investigation into the thermal performance and optimisation of a HBTMS for a battery pack comprising twelve 18,650 LIBs. The system integrated CPCM with liquid cooling and was evaluated under cyclic operating conditions consisting of 1C charging, a 5-min rest period, and 2C discharging at ambient temperatures up to 40 °C. The results demonstrated that the hybrid configuration significantly outperformed systems employing either PCM or liquid cooling alone, effectively maintaining the maximum cell temperature below 44.8 °C and the temperature difference under 2 °C. Huang et al. [23] investigated a HBTMS for 18,650 LIBs, incorporating PCM and expanded graphite with fin structures and forced-air cooling. Using a combination of experimental validation and numerical modelling, the system was assessed under cyclic conditions including 1C charge and 2C and 5C discharge at 25 °C. The optimal configuration was determined via a global sensitivity analysis using an adaptive Kriging-based high-dimensional model representation (HDMR), followed by a multi-objective optimisation. Results showed that the optimised HBTMS significantly reduced the maximum temperature and its variation by up to 38.72% and 40.09%, respectively, compared to the original design. While these investigations demonstrate promising cyclic thermal control, differences in modelling assumptions, boundary conditions, and performance metrics limit cross-study comparability and hinder the development of unified design guidelines.

Despite substantial progress in hybrid battery thermal management systems (HBTMSs), a clear gap persists in the simultaneous and systematically optimised integration of metal foam–enhanced active and passive cooling strategies. While several studies have examined conventional solid fins for augmenting PCM-based passive cooling, the thermal advantages of advanced geometries such as porous fins have been largely overlooked. Unlike solid fins, which primarily provide discrete and directionally conductive pathways for heat extraction, metal foam forms a three-dimensional interconnected ligament network within the PCM domain [6,24,25]. This porous topology reduces internal thermal resistance and promotes volumetric heat spreading rather than localised heat removal [26]. Similarly, in conventional liquid cooling-based BTMS, heat transfer is often limited by the progressive development of thermal boundary layers along channel walls. The insertion of porous media within cooling channels modifies this behaviour by inducing crossflow mixing and disrupting boundary layer reformation, thereby mitigating undesirable coolant temperature rise along the flow direction. In addition, the permeability of metal foam enables fluid penetration and interfacial solid–fluid heat exchange within the porous matrix, intensifying convective transport and improving overall cooling efficiency [27–29]. Consequently, metal foam provides coupled conduction–convection enhancement across both passive and active domains. Furthermore, most existing studies have explored individual design parameters in isolation, often lacking a systematic optimisation framework. To address these limitations, the present study introduces a novel HBTMS architecture that integrates PCM, porous fins, and liquid cooling, augmented by porous layers, to strengthen both passive and active cooling mechanisms. Building upon the authors' previous investigations [30,31], which analysed the thermal impact of various design features, this work advances the research by applying the Taguchi design of experiments (DOE) methodology to systematically rank the influence of key parameters on thermal performance. This study conducts a comprehensive evaluation of cyclic thermal behaviour, explicitly accounting for both discharge and charge phases using the optimal HBTMS. This aspect is particularly significant, as most previous studies have primarily focused on the discharge process due to its higher rate of heat generation within the battery. However, the thermal implications of the charging phase have received limited attention, despite its considerable contribution to the accumulated heat in the system during operating cycles.

2. Proposed HBTMS

The proposed HBTMS incorporates PCM, liquid cooling, and metal foam, which is employed both as embedded fins and layered inserts. As illustrated in Fig. 1, the battery module consists of twelve 18,650 LIBs. The metal foam serves two distinct thermal enhancement roles: it functions as longitudinal fins surrounding each cell within the PCM and as layers placed within copper tubes. Fig. 1 (a) presents a detailed view of the system's structural components. Each battery cell is enclosed in an aluminium housing to improve thermal distribution and eliminate direct contact between the PCM and the cell surface. To augment the thermal conductivity of the PCM, porous fins are inserted longitudinally, allowing paraffin to permeate their porous structure. As the active cooling part of the system, aluminium cooling plates embedded with copper tubes with porous layer inserts are employed, through which water circulates as the active coolant. Fig. 1 (b) provides the drawing of the HBTMS, including dimensions tailored for different cooling plate configurations.

The battery and PCM housings, together with the aluminium cooling plates, are compatible with metal powder bed fusion techniques such as selective laser melting (SLM) using AlSi10Mg alloy, enabling compact integration of internal cooling passages within a lightweight structural enclosure. Copper tubes are embedded within the cooling plates to provide liquid flow paths, while commercially available open-cell copper foam is machined to the required geometry and press-fitted into position as longitudinal fins within the PCM domain and as porous inserts inside the copper tubes. To minimise interfacial thermal contact resistance between assembled components, thermally conductive interface materials may be applied at the battery–housing and housing–metal foam interfaces to improve thermal continuity across mechanically joined regions. The aluminium housing thickness considered in the present design is 2 mm, consistent with lightweight structural design considerations.

For the present investigation, cylindrical 18,650 LIBs of the

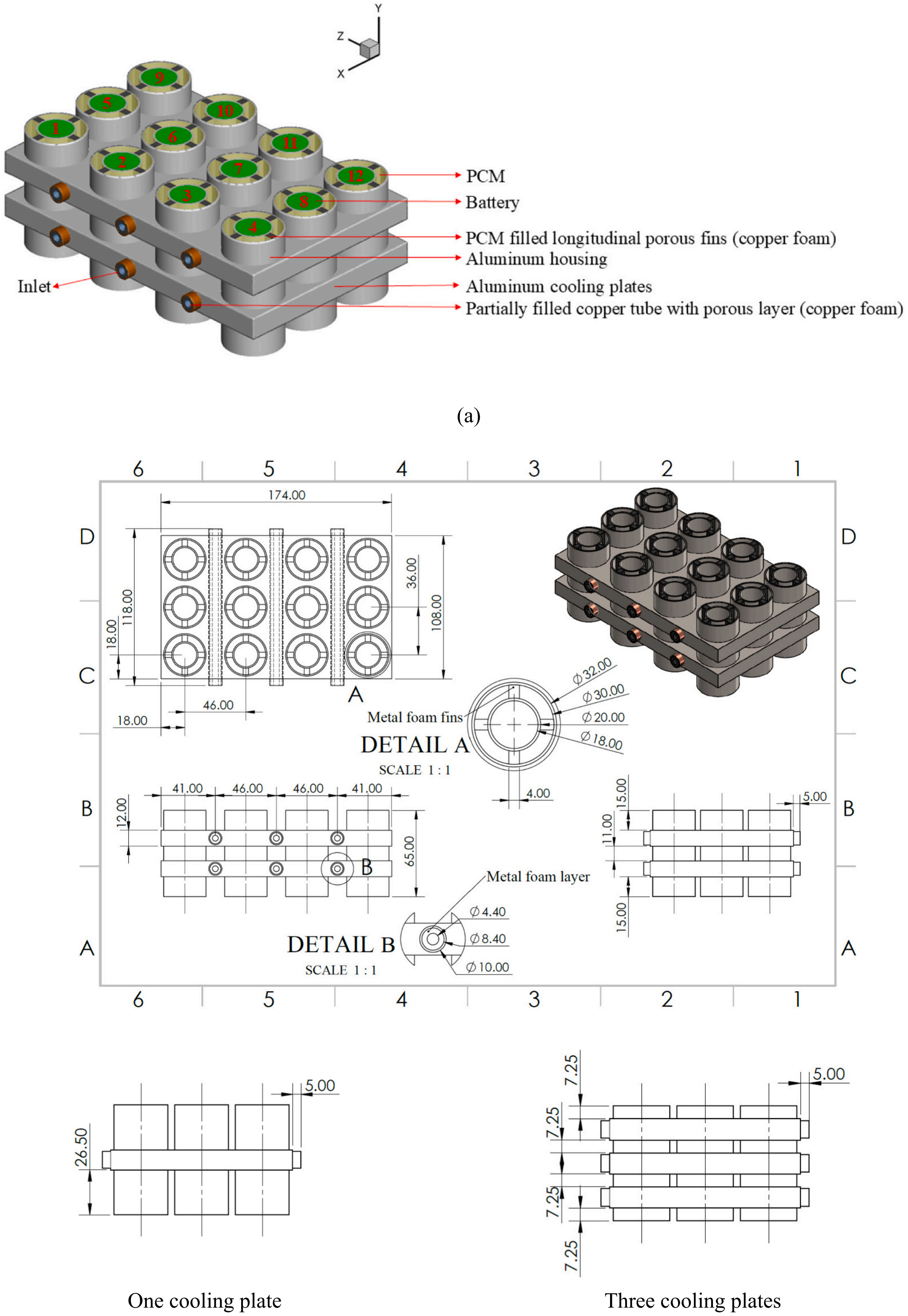

(a)

One cooling plate

Three cooling plates

(b)

Fig. 1. Proposed HBTMS in terms of (a) components of the system and (b) dimensional details shown in mm.

$LiNi_xCo_yMn_zO_2$ (NCM) chemistry were selected, owing to their high energy density and widespread use in electric vehicle applications [32]. The selected NCM cell has a nominal voltage of 3.7 V, a capacity of 2.6 Ah, and weighs 0.0475 kg. Its thermal properties include a radial thermal conductivity of 0.2 $W \cdot m^{-1} \cdot K^{-1}$, an axial thermal conductivity of 37.6 $W \cdot m^{-1} \cdot K^{-1}$, and a specific heat capacity of 1200 $J \cdot kg^{-1} \cdot K^{-1}$ [33]. All thermophysical properties of the utilised materials were adopted based on [30]. The thermophysical properties of all materials employed in this study are presented in Table 1.

3. Numerical modelling

3.1. Battery heat generation modelling

To reflect realistic operating conditions, the transient heat generation of the lithium-ion battery was taken into account. A lumped-

Table 1
Thermophysical properties of the materials [34,35].

Materials	Properties	Value
Al alloy	Thermal conductivity ($W \cdot m^{-1} \cdot K^{-1}$)	167
Al alloy	Specific heat capacity ($J \cdot kg^{-1} \cdot K^{-1}$)	896
Al alloy	Density ($kg \cdot m^{-3}$)	2700
Copper	Thermal conductivity ($W \cdot m^{-1} \cdot K^{-1}$)	387.6
Copper	Specific heat capacity ($J \cdot kg^{-1} \cdot K^{-1}$)	386
Copper	Density ($kg \cdot m^{-3}$)	8900
Paraffin	Thermal conductivity ($W \cdot m^{-1} \cdot K^{-1}$)	0.2
Paraffin	Specific heat capacity ($J \cdot kg^{-1} \cdot K^{-1}$)	2000
Paraffin	Density ($kg \cdot m^{-3}$), solid	880
Paraffin	Density ($kg \cdot m^{-3}$), liquid	760
Paraffin	Solidus temperature (K)	311.15
Paraffin	Liquidus temperature (K)	316.15
Paraffin	Latent heat ($J \cdot kg^{-1}$)	174,000
Paraffin	Dynamic viscosity ($Kg \cdot m^{-1} \cdot s^{-1}$)	0.02
Paraffin	Thermal expansion coefficient (K^{-1})	0.0001
Water	Thermal conductivity ($W \cdot m^{-1} \cdot K^{-1}$)	0.6
Water	Specific heat capacity ($J \cdot kg^{-1} \cdot K^{-1}$)	4182
Water	Density ($kg \cdot m^{-3}$), solid	998.2
Water	Dynamic viscosity ($Kg \cdot m^{-1} \cdot s^{-1}$)	0.001003

capacitance approach was adopted to model the time-dependent thermal response of the cell, incorporating both resistive (Joule) and entropic heat generation components. The validity of this model is determined by the Biot number (Bi), expressed as $Bi = hL_b/k_b$, where h denotes the convective heat transfer coefficient, L_b represents the characteristic length (calculated as the volume-to-surface-area ratio of the battery), and k_b is the thermal conductivity of the battery. The lumped-capacitance assumption holds when the Biot number is less than 0.1 [34]. Under these conditions, the battery is considered thermally homogeneous, with uniform internal temperature and material properties, while the rate of heat generation varies with temperature and discharge current [36]. The total heat generation is quantified using the Bernardi Eq. [33]:

$$Q_t = Q_{irr} + Q_{rev} \tag{1}$$

$$Q_{irr} = I(E - V) = I^2 R_e \tag{2}$$

$$Q_{rev} = -T\Delta S\left(\frac{I}{nF}\right) = -I\left[T\left(\frac{dE}{dT}\right)\right] \tag{3}$$

The total heat generation Q_t within the battery consists of two primary components: irreversible heat Q_{irr} and reversible heat Q_{rev}. These components are governed by various electrochemical and thermal parameters, including the open circuit voltage E, terminal voltage V, electric current I, temperature T, total internal resistance R_e, entropy change ΔS, number of electrons involved n, Faraday's constant F, and the entropy coefficient dE/dT. The Hybrid Pulse Power Characterization (HPPC) test [37] is widely used to characterise the functional dependencies of the internal resistance and entropy coefficient. In this study, the transient heat generation was modelled using experimental data reported in [33,38,39], and the governing equations were applied across discharge rates of 1C, 3C, and 5C.

The heat generation per unit of the battery volume (q_b) is defined as follows:

$$q_b = \frac{Q_t}{Vol._{battery}} \tag{4}$$

Since heat generation during charging is significantly lower than during discharging, limited experimental studies have reported detailed transient heat generation behaviour during the charging process. For the specific lithium-ion battery investigated in this study, to the authors' best knowledge, there is limited published transient charging heat generation data. Therefore, constant heat generation values based on experimental data from [23] were adopted for various charging C-rates. These values are summarised in Table 2 for different charge C-rates. It is acknowledged that charging heat generation in practice depends on state of charge (SOC), temperature, and internal resistance variations. The use of constant values therefore represents a modelling simplification that may slightly smooth transient temperature evolution during the charging phase. However, because the magnitude of charging heat generation is substantially lower than that during high-rate discharge, its influence on the overall cyclic thermal trends and maximum temperature behaviour is limited within the scope of the present study.

Table 2
18650 lithium-ion battery heat generation during charge [23].

C rate	q_b ($W.m^{-3}$)
1C	28,773
2C	78,957
3C	171,075

A transient volumetric heat generation term was implemented within the battery domain using a User Defined Function (UDF). During discharge, the heat generation rate was evaluated as a function of electric current, temperature, and state of charge (SOC), with SOC updated based on the simulation time. For discharge–rest–charge cycling, the source term was defined in a phase wise manner by tracking the elapsed time within each cycle and applying the corresponding heat-generation formulation for each operating phase.

3.2. Governing equations and boundary conditions

The enthalpy-porosity method was used to model the phase change behaviour of the PCM, where the mushy region, representing the coexistence of solid and liquid phases, is treated as a porous domain. This approach incorporates the latent heat effects directly into the energy conservation equation, eliminating the need to explicitly track the phase boundary [40,41]. In the case of pure PCM without copper foam, three distinct regions emerge during melting and solidification: solid, liquid, and mushy zones. Within the mushy region, the PCM is considered a porous medium, where the solid PCM serves as the matrix and the liquid portion occupies the pore space. In contrast, when simulating CPCMs integrated with copper foam, the liquid region is also represented as a porous medium, but with a porosity value different from that assigned to the mushy zone [42]. Copper foam was modelled as a porous medium using the Darcy–Brinkman–Forchheimer (DBF) approach. The local thermal equilibrium (LTE) model was applied to the porous fins surrounding the batteries, whereas the local thermal non-equilibrium (LTNE) model was employed for the porous layer inside the copper tubes to account for potential temperature differences between the solid and fluid phases. This configuration dependent selection of LTE and LTNE models was made based on validation against representative experimental studies, as discussed in Section 3.6, to balance predictive accuracy and computational efficiency. The initial temperature of the entire HBTMS domain was set equal to the ambient temperature. A mass flow inlet boundary condition was prescribed at the coolant inlet of the copper tubes with specified mass flow rate and inlet temperature according to the investigated operating case. A pressure outlet condition at atmospheric pressure was imposed at the tube exit. The bottom surface of the HBTMS was treated as adiabatic, while natural convection heat transfer to ambient air was applied on the remaining external surfaces using a constant convective heat transfer coefficient of 10 $W \cdot m^{-2} \cdot K^{-1}$. No-slip velocity boundary conditions were imposed at all solid walls. Laminar flow was assumed for both the clear tube region and porous inserts [30,31].

The principal modelling assumptions adopted in this study are as follows:

- The flow of molten PCM and coolant is unsteady, laminar, and incompressible.

- The PCM phases are assumed to be homogeneous and isotropic.
- The liquid PCM and water are treated as Newtonian fluids.
- The Boussinesq approximation is applied to account for buoyancy effects in natural convection.
- Volume change during PCM phase transition, viscous dissipation, and thermal radiation effects are neglected.
- Interfacial thermal contact resistance between adjoining solid components is neglected.
- The copper foam structure is assumed to be homogeneous and isotropic at the representative elementary volume scale.
- Local thermal equilibrium (LTE) is assumed between PCM and porous fins.
- Local thermal non-equilibrium (LTNE) is assumed between water and porous layers.

The governing equations were numerically solved using ANSYS FLUENT 23/R2. The solution employed specified initial and boundary conditions, with pressure–velocity coupling handled via the SIMPLE algorithm. Convective terms were discretised using a second-order upwind scheme, transient terms with a second-order implicit time integration scheme, and diffusion terms through spatial gradient reconstruction using the least squares cell-based method. Convergence criteria were set with residuals of 10^{-4} for continuity and momentum equations, and 10^{-6} for the energy equation.

3.3. Mesh and time-step independence analysis

The grid independence was assessed using the Grid Convergence Index (GCI) [43,44]. Three types of grid densities and their corresponding GCI calculations are presented in Table 3. The GCI for 6,612,690 grid cells is below 3% which meets the grid convergence index criterion [45]. Also, the generated mesh for the HBTMS is shown in Fig. 2.

Different time steps were studied to check time step independencies. Table 4 provides the maximum temperature of the battery surface at the end of 5C discharge for different time steps. As shown, a time step of 1 s was found to be appropriate for the current investigation.

3.4. Taguchi's design of experiments (DOE)

As shown in Table 5, the statistical analysis based on the Taguchi method involved 11 different factors, including the number of cooling plates, ambient temperature, coolant temperature, inlet mass flow rate, porous fin thickness, porous fin number, porous fin porosity, porous fin pore density, porous layer porosity, porous layer pore density, and porous layer thickness. These factors were systematically varied across three levels to investigate their impact on system performance. Considering 11 factors at three levels, an L27 (3ˆ11) orthogonal array was developed using the Taguchi method in Minitab software. As detailed in Table 6, this array was utilised to explore various HBTMS configurations while identifying the minimum number of required cases for an efficient analysis.

The L27 (3-level) orthogonal array provides 26 degrees of freedom (DOF). Since each three-level factor contributes two DOF, the 11 investigated factors account for a total of 22 DOF. The remaining four DOF were assigned to estimate experimental error, confirming that the total DOF of the selected design parameters remains within the allowable limit of the chosen orthogonal array and ensuring the statistical adequacy of the Taguchi design. Also, An ANOVA assessment indicated that the residual error contribution for all response variables remained below 10%, suggesting that the optimisation results are largely governed by main effects within the investigated parameter ranges.

During the data analysis phase, the outcomes associated with the objective functions are converted into Signal-to-Noise (S/N) ratios, which serve to assess the degree to which the observed results deviate from or align with the expected performance derived from simulations [46]. Depending on the nature of the objective function, one of three S/N ratio formulations is applied: “lower-the-better,” “higher-the-better,” or “nominal-the-best” [47]. In this study, the primary response variables include maximum battery surface temperature ($T_{Max,\ Sur}$), maximum temperature difference within the battery module (ΔT_{Max}), performance evaluation criteria (PEC), and energy density (E_d).

The PEC quantifies the relative improvement in heat transfer by comparing the Nusselt number and pressure drop in liquid cooling systems with and without copper foam layers and is defined as follows [48]:

$$PEC = \frac{\overline{Nu}/\overline{Nu}_0}{\left(\overline{f}_r/\overline{f}_{r0}\right)^{1/3}} \tag{5}$$

where $\overline{Nu}$ and $\overline{f}_r$ are the average Nusselt number for liquid cooling and friction factor, respectively, are defined as follows:

$$\overline{Nu} = \frac{\overline{h}D}{K_f} \tag{6}$$

where $\overline{h}$, D, and K_f represent the average convection heat transfer coefficient, copper tube inner diameter, and water thermal conductivity, respectively.

$$\overline{f}_r = \frac{\Delta P}{\rho_f U_{inlet}^2} \tag{7}$$

where ΔP, ρ_f, and U_{inlet} denote the pressure drop along the copper tube, water density, and inlet velocity, respectively.

In the present investigation, energy density is defined as a system-level gravimetric metric, calculated as the cell's nominal energy (UC_0) normalised by the mass of the HBTMS (m). It therefore quantifies the packaging mass penalty associated with the thermal management hardware, rather than the intrinsic electrochemical energy density of the cell. Since the nominal voltage and nominal capacity remain identical across the compared configurations, variations in energy density arise solely from differences in HBTMS mass [49]. The energy density is therefore expressed as:

$$E_d = \frac{UC_0}{m} \tag{8}$$

where E_d denotes the system-level gravimetric energy density (Wh/kg), U is the battery's nominal voltage (V), C_0 indicates the battery's nominal capacity (Ah), and m signifies the mass of the HBTMS (kg). The mass of each component is calculated from its geometric volume and material density. For porous copper foam regions, the effective solid mass is determined using the porosity-weighted solid fraction, thereby accounting only for the copper matrix contribution.

For Taguchi analysis of the $T_{Max,\ Sur}$, ΔT_{Max}, $1/\ E_d$, and $1/\ PEC$ the lower-the-better option was considered to optimise the HBTMS for better thermal performance. The formula for the lower-the-better S/N ratio is [50]:

$$S\Big/N = -10 \times \log_{10}\left(\frac{1}{n_{test}}\sum_{i=1}^{n_{test}} y_i^2\right) \tag{9}$$

The formula employs n_{test} to indicate the total number of test runs, while y_i denotes the value of the i^{th} performance parameter. In the context of this study, the y_i represent to the $T_{Max,\ Sur}$, ΔT_{Max}, $1/\ Ed$, and $1/\ PEC$ for each test.

Table 3
GCI analysis for different studied grids.

Grid number (N)	h_i	r	(f_i) $T_{Max,\ Sur}$ (K)	ε_r	GCI (%)
4,944,155	1	1.25	313.894287	0.052741	18.30
6,612,690	0.8	1.25	313.897891	0.003603	1.25
11,642,045	0.64	–	313.845152	–	–

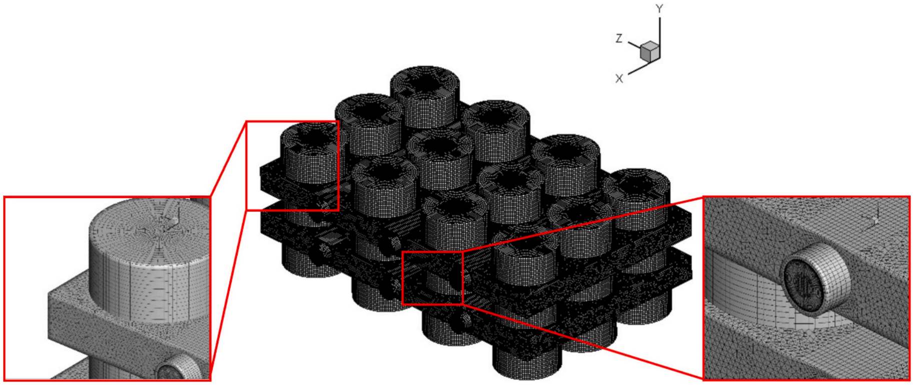

Fig. 2. Generated mesh for the HBTMS.

Table 4
Different time steps for time step independency study.

Time step (second)	$T_{Max,\ Sur}$ (K)	Error (%)
0.25	313.9788	–
0.5	313.9391	0.012635
1	313.8943	0.014271
2	313.7315	0.051876

Table 5
Factors and levels used in Taguchi method analysis.

Factors	Level 1	Level 2	Level 3
Number of cooling plates	1	2	3
Ambient temperature (K)	308.15	313.15	318.15
Coolant temperature (K)	298.15	303.15	308.15
Inlet mass flow rate (kg/s)	0.0002	0.001	0.002
Porous fin thickness (mm)	2	4	6
Porous fin number	4	6	8
Porous fin porosity	0.7	0.8	0.9
Porous fin pore density (PPI)	20	30	40
Porous layer thickness (mm)	4	5	6
Porous layer porosity	0.7	0.8	0.9
Porous layer pore density (PPI)	20	30	40

The results as the Taguchi response S/N ratio table offer a comprehensive analysis of the relative influence of each investigated factor on the selected response variables. Specifically, the level values correspond to the mean S/N ratios obtained for each distinct factor level, wherein higher S/N ratios indicate improved system performance or reduced variability in the measured response. Additionally, the Delta values, calculated as the difference between the maximum and minimum mean S/N ratios across the levels for each individual factor, serve as quantitative indicators of factor sensitivity or significance. Consequently, factors demonstrating larger Delta values are identified as having a more pronounced effect on the response of interest, whereas those with lower Delta values display limited influence. The associated parameter rankings, derived directly from the Delta values, facilitate prioritisation of influential factors, thereby guiding targeted optimisation strategies and subsequent system design enhancements [51].

3.5. *Cyclic charge and discharge performance of the HBTMS*

The performance of the HBTMS over 5 cycles of discharge, rest and charge has been evaluated and compared against pure PCM cooling. The specific C-rates for discharge and charge, along with the rest durations, are summarised in Table 7. Given that the highest heat generation occurs during the discharge phase, a high discharge rate of 5C has been selected for all cycle scenarios. The rest periods are defined in accordance with common practice in the literature [19,22,52], providing sufficient time for the battery to cool before the subsequent charging phase. For safety reasons, the maximum charging rate is limited to 3C, as recommended in prior studies [23]. The selection of five cycles is intended to evaluate short-term thermal regeneration stability rather than long-term electrochemical ageing.

3.6. *Validation*

The numerical methodologies employed in this study were validated by comparison with multiple experimental investigations. To validate the lumped-capacitance model, a single 18,650 cell configuration was simulated in accordance with the experimental conditions reported in [39]. The ambient temperature was set to 298.15 K to replicate the temperature-controlled chamber conditions. Natural convection was applied on all external battery surfaces using a constant convective heat transfer coefficient of 5 $W{\cdot}m^{-2}{\cdot}K^{-1}$. As illustrated in Fig. 3 (a), the battery surface temperature predictions were compared with the corresponding experimental measurements.

For validation of the porous fin model embedded within PCM, the experimental study of Hu et al. [53] was reproduced numerically. The aluminium foam–paraffin composite (porosity 0.75, pore density 10 PPI) was modelled according to the reported geometry and thermophysical properties. A constant heat flux of 3500 $W{\cdot}m^{-2}$ was imposed at the heated surface, while symmetry and natural convection boundary conditions ($h = 5\ W{\cdot}m^{-2}{\cdot}K^{-1}$) were applied to the remaining boundaries. The experimental temperature profiles were compared with numerical predictions obtained using both the LTE and LTNE models, as shown in Fig. 3 (b). While both approaches accurately predicted the CPCM temperature, the LTNE model provided marginally higher accuracy. Nevertheless, due to the similar predictive capability of the two models and the lower computational cost of the LTE approach, the LTE method was adopted for the simulations involving porous fins.

For the assessment of porous layers integrated within copper tubes, the experimental study by Amani et al. [54], which investigated water flow through a copper tube subjected to a constant wall heat flux of 100 $W{\cdot}m^{-2}$ and filled with copper foam (porosity 0.8 and pore density 10 PPI), was numerically replicated. The simulated average Nusselt number on the tube surface and the corresponding pressure drop were compared with the experimental measurements, as presented in Fig. 3 (c) and Fig. 3 (d), respectively. As depicted in Fig. 3 (c), the LTNE model achieved superior accuracy compared with the LTE approach; therefore, the LTNE model was selected for the simulation of the porous layers within the copper tube. Overall, the numerical predictions across different configurations demonstrate good agreement with the experimental data. Minor deviations, including partial underestimation in certain cases, may be attributed to idealised boundary assumptions, neglected thermal contact resistance, and inherent measurement uncertainties in the experimental setups. The calculated relative errors remain within acceptable bounds, demonstrating adequate agreement between

Table 6
L27 orthogonal array based on the Taguchi method.

Case	Number of cooling plates	Ambient temperature (K)	Coolant temperature (K)	Inlet mass flow rate (kg/s)	Porous fin thickness (mm)	Porous fin number	Porous fin porosity	Porous fin pore density (PPI)	Porous layer porosity	Porous layer pore density (PPI)	Porous layer thickness (mm)
1	1	308.15	298.15	0.0002	2	4	0.7	20	0.7	20	4
2	1	308.15	298.15	0.0002	4	6	0.8	30	0.8	30	5
3	1	308.15	298.15	0.0002	6	8	0.9	40	0.9	40	6
4	1	313.15	303.15	0.001	2	4	0.7	30	0.8	30	6
5	1	313.15	303.15	0.001	4	6	0.8	40	0.9	40	4
6	1	313.15	303.15	0.001	6	8	0.9	20	0.7	20	5
7	1	318.15	308.15	0.002	2	4	0.7	40	0.9	40	5
8	1	318.15	308.15	0.002	4	6	0.8	20	0.7	20	6
9	1	318.15	308.15	0.002	6	8	0.9	30	0.8	30	4
10	2	308.15	303.15	0.002	2	6	0.9	20	0.8	40	4
11	2	308.15	303.15	0.002	4	8	0.7	30	0.9	20	5
12	2	308.15	303.15	0.002	6	4	0.8	40	0.7	30	6
13	2	313.15	308.15	0.0002	2	6	0.9	30	0.9	20	6
14	2	313.15	308.15	0.0002	4	8	0.7	40	0.7	30	4
15	2	313.15	308.15	0.0002	6	4	0.8	20	0.8	40	5
16	2	318.15	298.15	0.001	2	6	0.9	40	0.7	30	5
17	2	318.15	298.15	0.001	4	8	0.7	20	0.8	40	6
18	2	318.15	298.15	0.001	6	4	0.8	30	0.9	20	4
19	3	308.15	308.15	0.001	2	8	0.8	20	0.9	30	4
20	3	308.15	308.15	0.001	4	4	0.9	30	0.7	40	5
21	3	308.15	308.15	0.001	6	6	0.7	40	0.8	20	6
22	3	313.15	298.15	0.002	2	8	0.8	30	0.7	40	6
23	3	313.15	298.15	0.002	4	4	0.9	40	0.8	20	4
24	3	313.15	298.15	0.002	6	6	0.7	20	0.9	30	5
25	3	318.15	303.15	0.0002	2	8	0.8	40	0.8	20	5
26	3	318.15	303.15	0.0002	4	4	0.9	20	0.9	30	6
27	3	318.15	303.15	0.0002	6	6	0.7	30	0.7	40	4

Table 7
Specifications of the investigated cycles.

Cycle type	Discharge rate	Rest time (s)	Charge rate
I	5C	300	1C
II	5C	300	2C
III	5C	300	3C

numerical predictions and experimental observations.

4. Results and discussion

4.1. Multi-objective optimisation and evaluation of HBTMS design parameters

Based on the developed L27 (3ˆ11) orthogonal array, 27 different HBTMS cases were simulated at a high 5C discharge rate. The results (response variables) at the end of the discharge (720 s) are presented in Table 8. The results include the maximum battery surface temperature ($T_{Max,\ Sur}$), maximum temperature difference within the battery module (ΔT_{Max}), performance evaluation criteria (PEC), reciprocal of performance evaluation criteria (1/PEC), energy density (E_d), reciprocal of energy density ($1/E_d$), and PCM liquid fraction (L_f). These data were systematically analysed to identify the most influential parameters affecting the proposed HBTMS and to optimise its design in terms of both thermal performance and energy density.

As depicted in Table 8, the lowest $T_{Max,\ Sur}$ of 311.3737 K was observed in case 12 for the HBTMS with two cooling plates, four porous fins (porosity of 0.8 and pore density of 40 PPI) with thickness of 6 mm, porous layer (porosity of 0.7 and pore density of 30 PPI) with thickness of 6 mm at ambient temperature of 308.15 K and water inlet with mass flow rate of 0.002 kg/s at 303.15 K. This low $T_{Max,\ Sur}$, as shown in Fig. 4 (c), was achieved due to the highest mass flow rate and porous layer thickness among different cases which improves the convective cooling within the copper tubes. The thicker porous layer enhances active cooling by increasing the solid–fluid interfacial area and promoting local thermal dispersion, thereby strengthening convective heat extraction. Simultaneously, thicker porous fins provide more effective conduction path between the battery and the PCM housing. Under these conditions, heat is preferentially transferred to the coolant before a significant PCM volume reaches the phase change temperature range; consequently, the PCM primarily acts as a secondary thermal buffer with limited latent heat participation. Given the substantial influence of ambient temperature on HBTMS performance, the lowest value among the different simulation cases was selected for analysis. Moreover, the lowest L_f was also observed in this case with the value of 1.48×10^{-6} and as illustrated in Fig. 4 (c), the PCM has remained unmelted around the batteries as the battery surface temperature is fairly close to the PCM melting temperature of 311.15 K. This phenomenon is attributed to the highest mass flow rate in the liquid cooling system, the greatest porous fin thickness, and the low ambient temperature. These factors enhanced heat dissipation from the system, reducing heat storage within the PCM and consequently lowering the thermal load on the HBTMS.

The highest $T_{Max,\ Sur}$ of 322.9469 K was achieved in case 7 for the HBTMS with one cooling plate, four porous fins (porosity of 0.7 and pore density of 40 PPI) with thickness of 2 mm, porous layer (porosity of 0.9 and pore density of 40 PPI) with thickness of 5 mm at ambient temperature of 318.15 K and water inlet with mass flow rate of 0.002 kg/s at 308.15 K. As depicted in Fig. 4 (a), $T_{Max,\ Sur}$ is mostly evident on the batteries 1, 4, 5, 8, 9, and 12 which are located away from the copper tubes. This $T_{Max,\ Sur}$ is a result of considering HBTMS with one cooling plate at the highest ambient and water inlet temperature along with the lowest number of porous fins with lowest thickness among the different cases. The combination of a high coolant inlet temperature and limited conduction path within the PCM due to fins number and thickness reduces the temperature gradient available for heat removal through the cooling plates. This shifts a larger fraction of the thermal burden to the PCM near the batteries, accelerating local melting. Also, in this case the HBTMS is experiencing high thermal load due to high ambient temperature. As shown in Fig. 4 (b), the highest L_f was recorded for this case and the PCM is fully melted as the ambient temperature is 7 K higher than PCM melting temperature. In this case as the PCM latent heat is

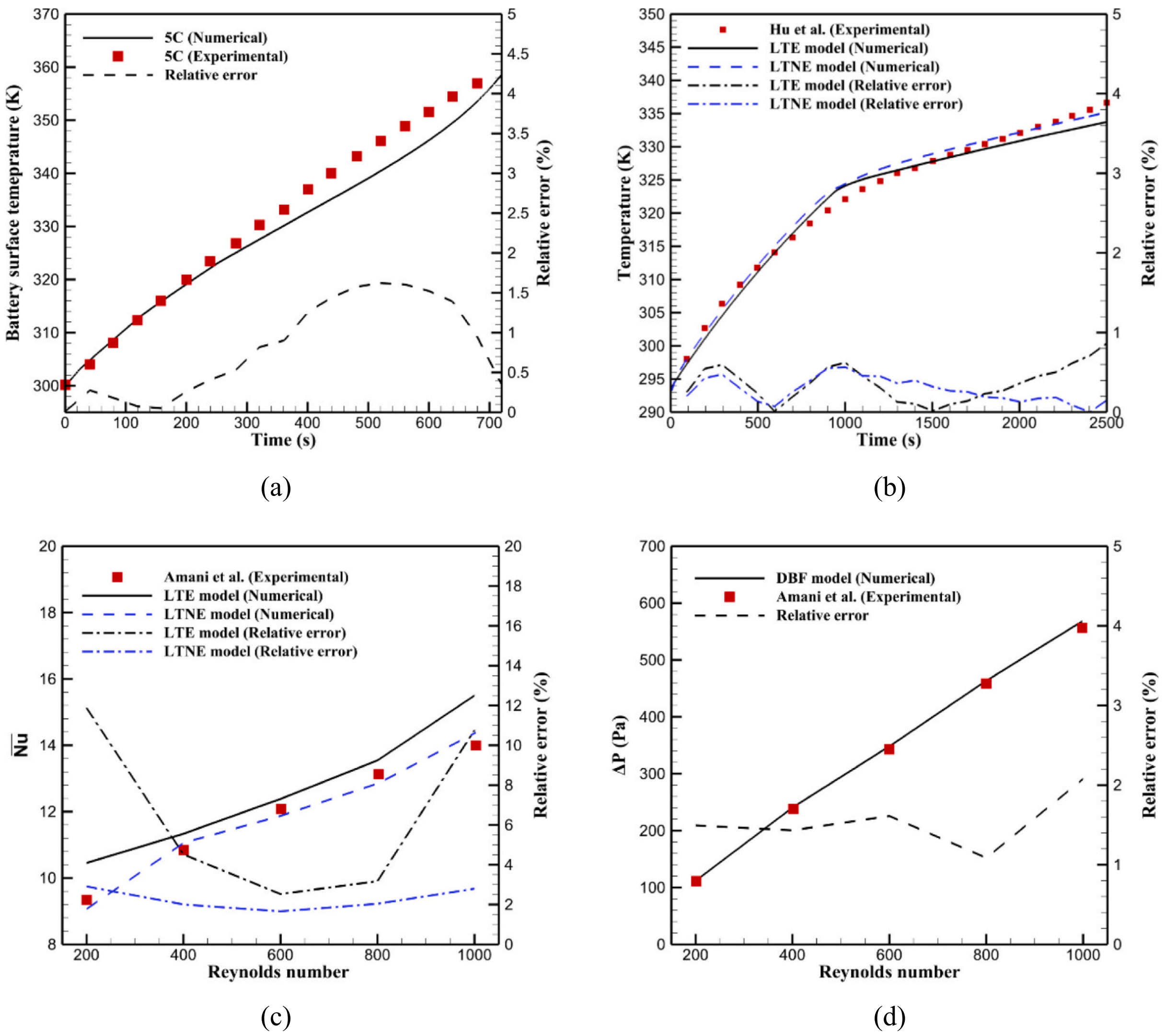

(a) (b)

(c) (d)

Fig. 3. Comparison of the present numerical results with experimental data for: (a) battery surface temperature measurements [39], (b) PCM-filled metal foam temperatures [53], (c) average Nusselt number [54], and (d) pressure drop [54].

fully utilised and due to thermal saturation [16], it is not able to absorb more heat through its latent heat. Also, the liquid cooling was not able to extract the generated heat effectively to prevent complete melting of PCM even at the highest mass flow rate since the inlet temperature was assumed to be high. This phenomenon is mentioned to be premature melting [46,55] that has to be avoided by improving the design of the HBTMS at high operational temperature.

The lowest ΔT_{Max} of 0.5843, according to Table 8, was observed in case 13 for the HBTMS involving two cooling plates, six porous fins (porosity of 0.9 and pore density of 30 PPI) with thickness of 2 mm, porous layer (porosity of 0.9 and pore density of 20 PPI) with thickness of 6 mm at ambient temperature of 313.15 K and water inlet with mass flow rate of 0.0002 kg/s at 308.15 K. Thermal systems based on liquid cooling beside their effective cooling has a drawback of an increased coolant temperature increase along the cooling channels specially at high flow rates which results in nonuniform temperature distribution. In this case the relatively low mass flow rate of the water contributes to achieving more uniform temperature which is evident in static temperature contour plots in Fig. 4 (e). A lower flow rate also reduces inlet dominated overcooling and weakens streamwise coolant temperature gradients within the cooling channels, thereby mitigating flow maldistribution effects at the module scale. Also, as the PCM L_f has reached 0.6528, it is not fully melted and as shown Fig. 4 (f) is mostly melted within the porous fins. As the PCM is not fully melted and experiencing phase changes, its thermal regulation capability is more dominant which also contributes to better temperature uniformity. In contrast the highest ΔT_{Max} of 4.5866, is still below the threshold of 5 K, that was recorded for case 22. This was for the HBTMS involving three cooling plates, eight porous fins (porosity of 0.8 and pore density of 30 PPI) with thickness of 2 mm, porous layer (porosity of 0.7 and pore density of 40 PPI) with thickness of 6 mm at ambient temperature of 313.15 K and water inlet with mass flow rate of 0.002 kg/s at 298.15 K. As shown in Fig. 4 (g), the temperature difference on the batteries' surface could be observed especially on batteries 2 and 3 that are located close to the cooling plates inlet. Cooling with high mass flow rate and very low inlet temperature compared to ambient temperature with three cooling plates in this case has caused unfavourable temperature gradient on batteries' surface. This behaviour is consistent with cooling maldistribution that the cells near the inlet experience stronger local convection because of the larger coolant-to-wall temperature difference, whereas downstream regions receive warmer coolant and therefore weaker heat extraction. The resulting non-uniformity increases ΔT_{Max} even though the absolute cooling capacity is high. Also, in contrast to case 13, Fig. 4 (g) indicates more localised PCM melting in case 22, suggesting non-uniform latent heat utilisation across the module. Thus, despite strong cooling near the inlet, the combined effect of inlet-biased cooling and uneven PCM

Table 8
Results of simulations for different cases based on L27 orthogonal array.

Case	$T_{Max,\ Sur}$ (K)	ΔT_{Max} (K)	PEC	1/PEC	E_d(Wh. kg^{-1})	1/E_d (kg.Wh^{-1})	L_f
1	313.9159	1.0689	1.3348	0.7491	72.8	0.0137	0.1825
2	313.1753	1.1032	1.2831	0.7793	69.8	0.0143	0.1687
3	313.8055	1.7866	1.1481	0.8709	70.2	0.0142	0.2975
4	315.1933	2.4667	1.3724	0.7286	73.1	0.0136	0.3930
5	315.2415	1.1828	1.1941	0.8373	70.5	0.0141	0.5814
6	315.0219	2.4853	0.6621	1.5103	69.1	0.0144	0.4801
7	322.9469	3.0728	1.1891	0.8409	74.9	0.0133	1
8	317.8275	3.7208	0.9771	1.0234	69	0.0144	0.8740
9	321.0093	3.1112	1.3695	0.7301	70	0.0142	0.9996
10	312.2005	1.4355	1.6579	0.6031	62	0.0161	0.0043
11	312.2411	0.9696	1.2137	0.8238	54.8	0.0182	0.0389
12	311.3737	2.6836	0.8209	1.2181	57.6	0.0173	1.48×10^{-6}
13	316.1688	0.5843	1.2894	0.7755	62.6	0.0159	0.6528
14	315.2296	0.6051	1.4787	0.6762	53.6	0.0186	0.6179
15	315.5884	0.7704	1.4426	0.6931	58.2	0.0171	0.6029
16	316.9885	2.9921	0.6876	1.4542	60.8	0.0164	0.7697
17	316.0834	3.7835	1.3181	0.7587	53.9	0.0185	0.6618
18	315.5619	3.4334	1.9125	0.5228	59.1	0.0169	0.6033
19	313.4588	0.5979	1.1808	0.8468	52.1	0.0191	0.0072
20	313.0146	0.7339	0.6952	1.4382	51.2	0.0195	0.0072
21	312.396	0.7467	1.2958	0.7717	45.9	0.0217	0.0073
22	311.8159	4.5866	0.4078	2.4517	49.8	0.0200	0.0072
23	312.3606	2.6788	1.2828	0.7795	52.4	0.0190	0.0072
24	312.6778	2.2751	1.1477	0.8712	46.9	0.0213	0.0072
25	320.8838	1.8304	1.2206	0.8192	51	0.0196	0.0072
26	321.2677	1.8471	1.1425	0.8752	53.1	0.0188	0.0072
27	320.1197	1.8658	1.3114	0.7625	45.5	0.0219	0.0072

participation leads to poorer temperature uniformity.

The highest PEC value of 1.91 is recorded in case 18 for the HBTMS involving two cooling plates, four porous fins (porosity of 0.8 and pore density of 30 PPI) with thickness of 6 mm, porous layer (porosity of 0.9 and pore density of 20 PPI) with thickness of 4 mm at ambient temperature of 318.15 K and water inlet with mass flow rate of 0.001 kg/s at 298.15 K. In this case the pressure drop was minimised due to the lowest porous layer thickness and highest porosity at moderate mass flow rate among other simulated cases. Also, the generated heat is transferred effectively by the porous fins with the highest thickness to the copper tubes with the lowest inlet temperature. Therefore, in this case the effective force convection was provided by the partially filled copper tubes with minimum pressure drop leading to the highest PEC value. In contrast, the lowest PEC value of 0.4078 was observed in case 22 for the HBTMS with three cooling plates, eight porous fins (porosity of 0.8 and pore density of 30 PPI) with thickness of 2 mm, porous layer (porosity of 0.7 and pore density of 40 PPI) with thickness of 6 mm at ambient temperature of 313.15 K and water inlet with mass flow rate of 0.002 kg/s at 298.15 K. This low PEC value in this case is the result of the highest thickness for the porous layer with the lowest porosity at the highest inlet mass flow rate. This resulted in the highest pressure drop, which outweighed the heat transfer enhancement provided by the insertion of the porous layer within the copper tubes.

Overall, the thermal performance metrics reveal two distinct trade-offs. First, improving $T_{Max,Sur}$ does not necessarily improve ΔT_{Max}, as stronger cooling in terms of high mass flow rate and low coolant inlet temperature, can intensify inlet to outlet cooling nonuniformity and increase temperature gradients across the module. Second, improving heat transfer enhancement does not always improve PEC, since the gain in convection and conduction may be offset by a disproportionate increase in pressure drop, especially for thick, low porosity porous layers at high flow rates. Accordingly, $T_{Max,Sur}$, ΔT_{Max}, and PEC should be interpreted as complementary rather than interchangeable indicators of thermal performance.

In terms of the E_d, the highest value of 74.9 was achieved in case 7 for the HBTMS with one cooling plate, four porous fins (porosity of 0.7 and pore density of 40 PPI) with thickness of 2 mm, porous layer (porosity of 0.9 and pore density of 40 PPI) with thickness of 4 mm. This case had the lowest cooling plate number, fin number and thickness and highest porosity of the porous layer. The lowest energy density value of 45.5 was recorded for case 27 for the HBTMS with three cooling plate, six porous fins (porosity of 0.7 and pore density of 30 PPI) with thickness of 6 mm, porous layer (porosity of 0.7 and pore density of 40 PPI) with thickness of 4 mm. In this case, the increased system weight is primarily due to the high number of cooling plates, each incorporating the maximum number of porous fins with the lowest porosity in both the fins and the porous layers.

In contrast to the thermal metrics, E_d is governed primarily by the mass penalty of added hardware including the cooling plates and porous structures rather than by the instantaneous heat transfer mechanisms. Consequently, configurations that improve thermal control through increased cooling plate number, fin thickness, or lower porosity foam may incur a measurable energy density penalty. This distinction is important as a thermally superior configuration may be less attractive at pack level if the thermal gains are achieved through disproportionate increases in structural mass. The optimisation therefore seeks a balanced design in which porous media are used to enhance local heat transfer efficiently, so that comparable thermal performance can be achieved with fewer or lighter components.

In order to study the influence of different factors simultaneously on the response variables, Taguchi analysis was caried out on $T_{Max,\ Sur}$, ΔT_{Max}, 1/PEC, and 1/E_d based on lower-the-better option. The "mean of means" method serves as a comprehensive measure for evaluating performance across multiple response variables, providing a structured approach to analysing complex systems with numerous performance criteria. This technique involves calculating the average of the mean responses for each factor level across all response variables, thereby assigning equal weighting to all response variables and facilitating a clearer assessment and comparison of different factor levels. By aggregating data in this manner, decision-making in multi-objective optimisation scenarios is simplified, and the most effective factor settings can be identified more efficiently. The magnitude of the mean of means, whether higher or lower, indicates the collective influence of a factor level on all response variables simultaneously.

As depicted in Fig. 5, for different number of cooling plates, the minimum value of mean of means was observed for two cooling plates.

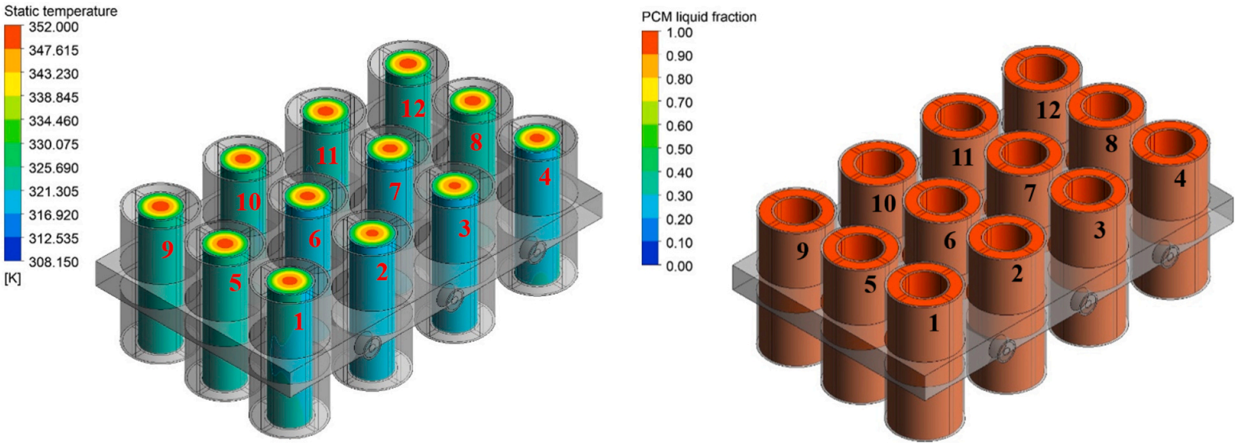

(a) (b)

Case 7

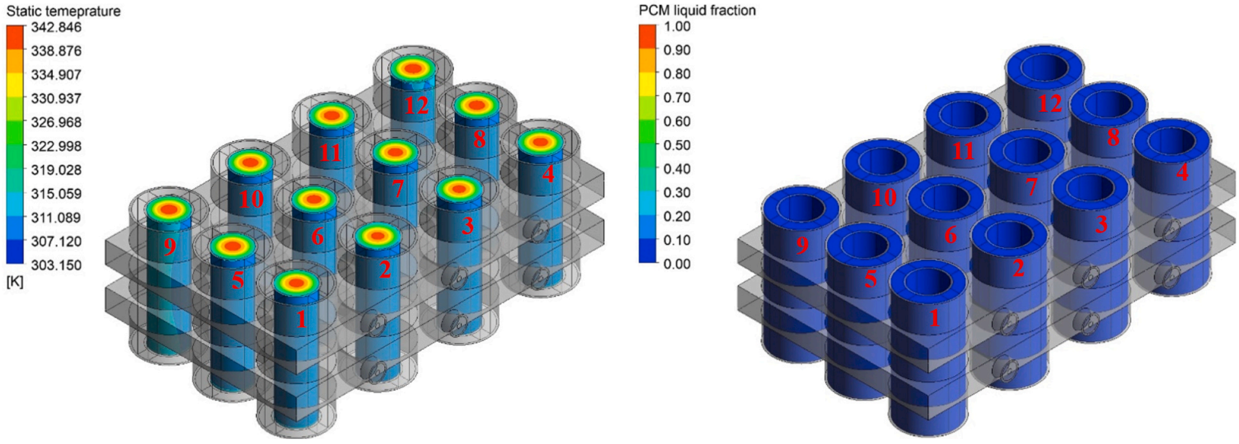

(c) (d)

Case 12

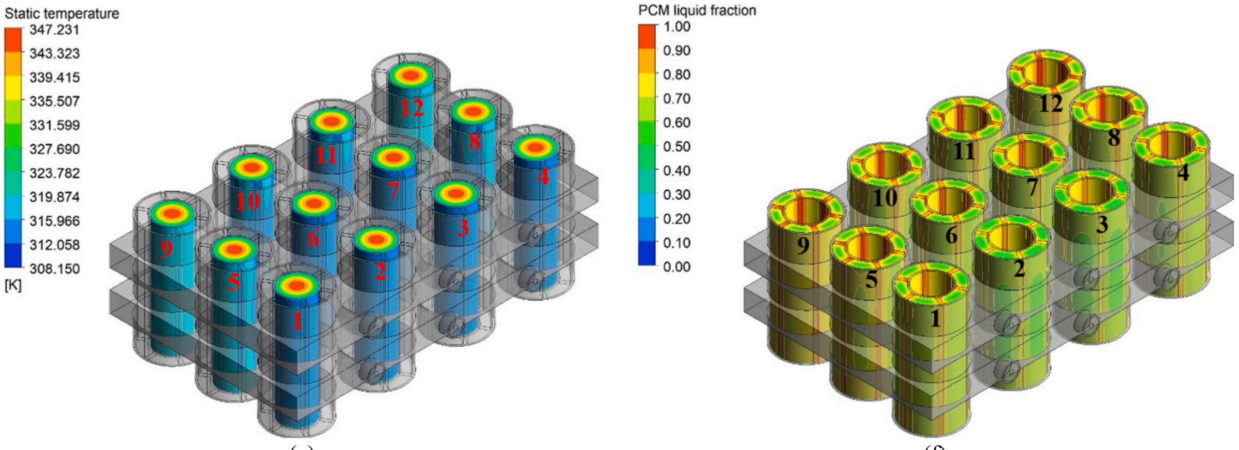

(e) (f)

Case 13

Fig. 4. Static temperature and PCM liquid fraction contour plots at the end of the 5C discharge for different cases.

Two cooling plates provide a balanced heat transfer performance by effectively controlling PCM melting and enabling active cooling for the HBTMS. This configuration significantly contributes to minimising $T_{Max,Sur}$ and ΔT_{Max}, and improving the PEC. Additionally, maintaining a moderate number of two cooling plates ensures an acceptable E_d while enhancing thermal performance. Regarding ambient temperature, the optimal case was achieved at the lowest ambient temperature of 308.15 K, as the reduced thermal load on the HBTMS facilitates better thermal management by lowering maximum temperature and improving temperature uniformity. Furthermore, active cooling was found to be more effective at lower ambient temperatures, leading to enhanced PEC value. Similarly, the lowest coolant inlet temperature of 298.15 K yielded a superior thermal performance by minimising $T_{Max,Sur}$ and ΔT_{Max}, and 1/PEC, as the cooling capability of the HBTMS is enhanced. For the inlet mass flow rate, a moderate value of 0.001 kg/s was found to be optimal, as it improves thermal performance in terms of $T_{Max,Sur}$ and ΔT_{Max} while

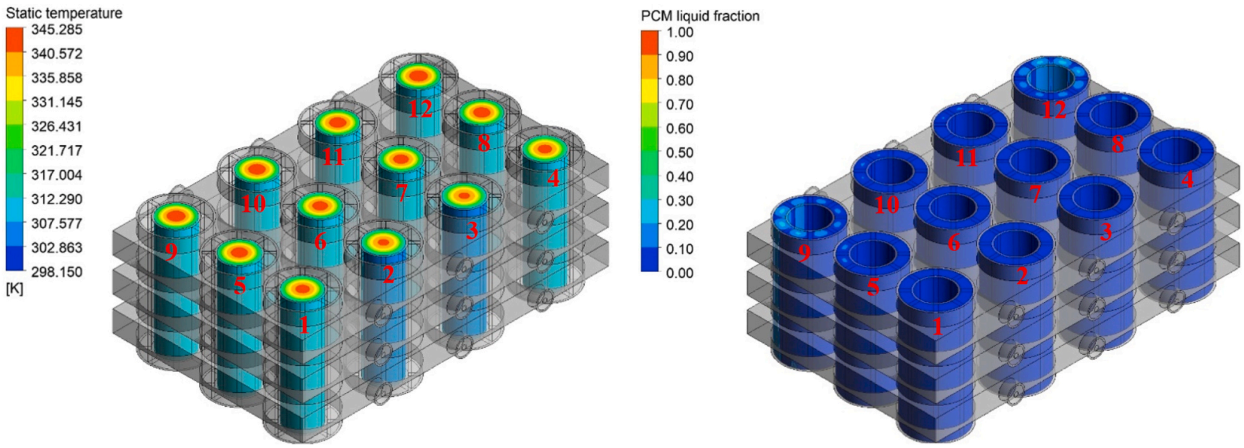

(g)	(h)

Case 22

Fig. 4. (*continued*).

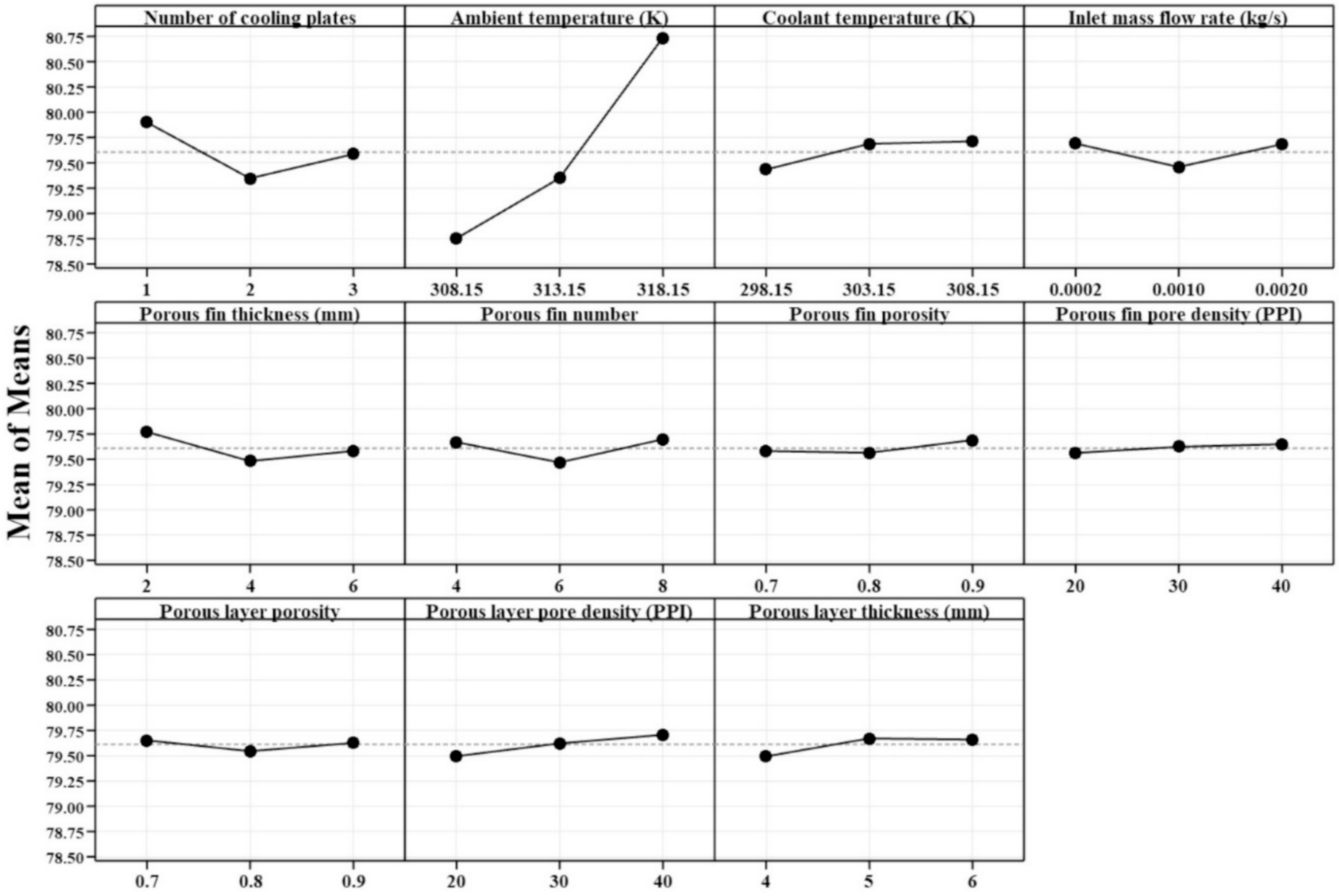

Fig. 5. Mean of means for various factors and levels at the end of the 5C discharge rate.

controlling the pressure drop to enhance PEC. These trends further confirm that the optimal setting is not the one with the strongest cooling intensity in every parameter, but the one that balances latent heat utilisation, coolant heat extraction, temperature uniformity, and hydraulic losses while limiting the associated mass increase.

A moderate fin thickness of 4 mm was found to be more effective in enhancing conduction within the PCM, leading to optimised $T_{Max,Sur}$, ΔT_{Max}, and PEC. Additionally, an optimised structural design could be achieved to maximise E_d. Similarly, a design incorporating a moderate number of six porous fins was identified as optimal, achieving the best performance in terms of $T_{Max,Sur}$, ΔT_{Max}, and PEC by optimising conduction paths within the PCM while maintaining a lightweight structure to enhance E_d. The mean of means value exhibited minor variations across different porous fin porosities, with a maximum fluctuation of 0.1. The minimum value was recorded at a porosity of 0.8, as this configuration provided the highest conduction within the PCM, resulting in optimised $T_{Max,Sur}$, ΔT_{Max}, and PEC. However, this type of porous fin slightly increased the overall system weight. A similar trend was observed for porous fin pore density, with maximum variations of 0.01, and the minimum value recorded at a pore density of 20 PPI.

Limited impact of porous layer porosity on the mean of means value was observed, with a moderate porosity of 0.8 leading to the optimised case. Similarly, the pore density of the porous layer demonstrated minimal influence, with variations of up to 0.1, and a low pore density of 20 PPI was identified as the optimal configuration. Since an increased porous layer thickness result in a higher pressure drop within the system and reduces the active cooling capability of the HBTMS, a porous layer thickness of 4 mm was determined to be the optimised design.

Table 9 summarises the Taguchi S/N ratios for the “mean of means,” evaluating the overall system response to each investigated factor across three distinct levels. Among the tested parameters, ambient temperature emerges as the most influential factor, exhibiting the largest Delta value of 0.17. This finding highlights the critical role of ambient temperature in determining the overall thermal performance of the battery system, with lower ambient temperatures generally improving system effectiveness. Following this, coolant temperature and inlet mass flow rate exhibit moderate yet notable impacts, with Delta values of 0.06 and 0.05, respectively, underscoring the importance of carefully controlling coolant conditions to optimise thermal management. Similarly, the number of cooling plates demonstrates a moderate influence with Delta value of 0.05, reinforcing that an optimal number of cooling plates contributes meaningfully to system performance. Conversely, parameters relating to porous structures such as porous layer porosity (Delta = 0.02), porous fin thickness (Delta = 0.02), porous fin porosity (Delta = 0.02), porous layer thickness (Delta = 0.02), porous layer pore density (Delta = 0.01), porous fin number (Delta = 0.01), and porous fin pore density (Delta = 0.01), showed comparatively minor influences. These results indicate that the porous media properties primarily serve to fine-tune the system's thermal performance, whereas external conditions including ambient temperature, coolant temperature, and inlet mass flow rate, represent the most critical parameters for overall optimisation.

4.2. Cyclic performance of the proposed HBTMS

In this section, the performance of the HBTMS over 5 cycles of discharge, rest and charge has been evaluated and compared against pure PCM cooling. The optimised HBTMS configuration identified in the previous section has been adopted for these cyclic performance studies, with a different coolant inlet temperature. This configuration comprises two cooling plates, an ambient temperature of 308.15 K, a coolant temperature of 303.15 K, and an inlet mass flow rate of 0.001 kg/s. Additionally, the system includes six porous fins with a thickness of 4 mm, a porosity of 0.8, and a pore density of 20 PPI, as well as a porous layer characterised by a thickness of 4 mm, a porosity of 0.8, and a pore density of 20 PPI.

4.2.1. Type I cycles (charging at 1C and discharging at 5C)

As depicted in Fig. 6 (a), under Type I cycles, the pure PCM cooling system reached $T_{Max,Sur}$ of 321.821 K at the end of the first cycle's discharge phase. This temperature subsequently decreased during the rest and charging phases due to the lower heat generation associated with 1C charging, in contrast to the 5C discharge. Fig. 6 (b) demonstrates that during the first cycle, the PCM melted to L_f value of approximately 0.44, and then partially solidified by the end of the cycle, reaching L_f of about 0.32. This indicates that the latent heat capacity consumed during the first cycle was not fully recovered. In contrast, the HBTMS recorded a $T_{Max,Sur}$ that was 9.6 K lower than that of the pure PCM system at the end of the first cycle's discharge. Due to the lower heat generation rate of the 1C charging phase and the enhanced heat removal capability of the HBTMS, $T_{Max,Sur}$ decreased significantly during the rest and charging stages, dropping even below the ambient temperature of 308.15 K by the end of the first cycle. As illustrated in Fig. 6 (b) and Fig. 7 (c), the HBTMS resulted in a lower degree of PCM melting during the first cycle, and the melted PCM was fully solidified by the end of the cycle, demonstrating complete restoration of the latent heat capacity.

As illustrated in Fig. 6 (a), the pure PCM cooling system exhibits a progressive increase in $T_{Max,Sur}$ across successive Type I cycles, reaching values of 321.821 K, 327.017 K, 329.490 K, 330.656 K, and 331.219 K from the first to the fifth cycle, respectively. The safety threshold of 323.15 K is exceeded during the second cycle, with the $T_{Max,Sur}$ rising to approximately 8 K above the limit in later cycles. Additionally, as shown in Fig. 6 (b), the PCM undergoes melting during each cycle but fails to fully solidify by the end of the rest and charging phases. In the final two cycles, the PCM becomes fully melted and saturated by the end of discharge. Over the five Type I cycles, the L_f peaks at approximately 0.74, indicating only partial restoration of the latent heat capacity. This incomplete phase change, as depicted in Fig. 7 (d) and (h), leads to localised melting around the battery cells. The resulting heat accumulation and elevated temperatures are primarily attributed to the PCM's low thermal conductivity and inadequate post cycle cooling.

In contrast, as shown in Fig. 6 (a), the HBTMS maintains a consistent pattern for $T_{Max,Sur}$ across multiple cycles, effectively preventing heat accumulation. This stability is also reflected in the PCM melting and solidification behaviour illustrated in Fig. 6 (b). The $T_{Max,Sur}$ of 312.215 K at the end of the first cycle slightly decreases to 312.183 K in subsequent cycles, due to the lower initial temperatures in cycles two to five, which fall below the ambient temperature. This contrasts with the pure PCM system, where the initial temperature of each cycle progressively increases, particularly during the first two cycles. Compared to the safety limit of 323.15 K, the HBTMS consistently maintains $T_{Max,Sur}$ approximately 11 K lower, indicating effective and reliable thermal management even over extended cycles. Furthermore, as shown in Fig. 7 (a) and (e), the temperature difference between the battery core and surface remains stable at less than 5 K after both the first and fifth cycles, highlighting the system's thermal uniformity. The effective temperature control achieved by the HBTMS is due to enhanced PCM thermal conductivity via embedded porous fins, which expand the active phase change region, and improved heat extraction through the porous layers in copper tubes. Additionally, as demonstrated in Fig. 6 (b) and Fig. 7 (c) and (g), unlike the pure PCM system, in which the liquid fraction increases by approximately 30% with each cycle, the HBTMS enables complete PCM solidification at the end of each cycle. This ensures full recovery of the latent heat capacity and supports stable, repeatable phase change behaviour. This HBTMS facilitates reversible and stable

Table 9

Response table for signal to noise ratios (S/N) for each level of factors for mean of means.

Level	Number of cooling plates	Ambient temperature (K)	Coolant temperature (K)	Inlet mass flow rate (kg/s)	Porous fin thickness (mm)	Porous fin number	Porous fin porosity	Porous fin pore density (PPI)	Porous layer porosity	Porous layer pore density (PPI)	Porous layer thickness (mm)
1	−43.99	−43.89	−43.92	−43.99	−43.97	−43.96	−43.96	−43.95	−43.95	−43.95	−43.96
2	−43.93	−43.93	−43.97	−43.94	−43.95	−43.95	−43.95	−43.96	−43.96	−43.96	−43.97
3	−43.95	−44.06	−43.98	−43.94	−43.95	−43.96	−43.97	−43.96	−43.97	−43.96	−43.95
Delta	0.05	0.17	0.06	0.05	0.02	0.01	0.02	0.01	0.02	0.01	0.02
Rank	4	1	2	3	6	10	7	11	5	9	8

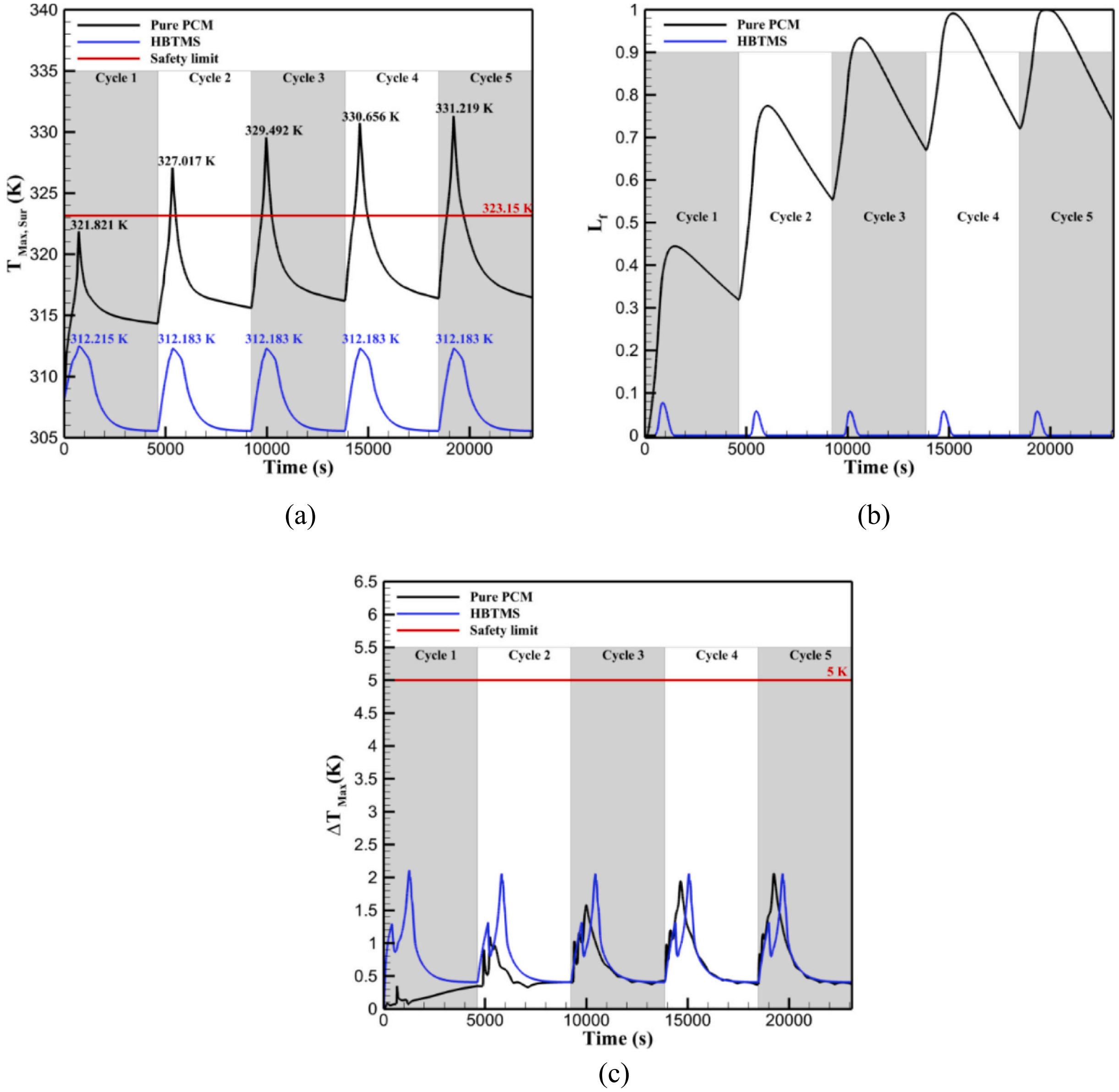

Fig. 6. Performance of the HBTMS under Type I cycles in terms of (a) maximum battery surface temperature, (b) PCM liquid fraction, and (c) maximum temperature difference within the battery module.

phase change dynamics along with continued phase change participation which results in vital thermal sustainability providing long-term durability of the system.

The performance of the HBTMS and the pure PCM cooling system in terms of the ΔT_{Max} is compared in Fig. 6 (c). As illustrated, both systems exhibit fluctuations in ΔT_{Max} across the cycles; however, in all cases, the values remain well below the safety threshold of 5 K. For the pure PCM system, ΔT_{Max} shows a gradual increase over successive cycles, reaching a peak value of approximately 2 K during the last two cycles. This increase corresponds to the progressive thermal saturation of the PCM, which limits the active melting region, as shown in Fig. 6 (b). In contrast, the HBTMS exhibits a consistent ΔT_{Max} pattern across all cycles, with a stable peak value of 2 K. This repeatable behaviour reflects the stable and reversible phase change dynamics of the PCM in the HBTMS configuration, as also demonstrated in Fig. 6 (b). Notably, each HBTMS cycle features two distinct ΔT_{Max} peaks. The first occurs immediately after the discharge phase, where the highest heat generation rate was observed and the effectiveness of liquid cooling varies across battery locations. A slight decrease follows during the rest period, when heat generation ceases and the HBTMS remains active in cooling. As charging begins, ΔT_{Max} increases again due to continued, though lower, heat generation. However, the HBTMS effectively mitigates this rise, leading to a gradual reduction in ΔT_{Max} through the charging phase and into the end of the cycle. Furthermore, both systems achieve a similar minimum ΔT_{Max} value of approximately 0.5 K at the end of each cycle.

4.2.2. Type II cycles (charging at 2C and discharging at 5C)

The performance of the HBTMS under Type II cycles is illustrated in Fig. 8 and compared with that of the pure PCM cooling. As shown in Fig. 8 (a), similar to the Type I cycles, the pure PCM system reaches a $T_{Max,Sur}$ approximately 1.33 K below the safety limit by the end of the first discharge. A subsequent temperature drop is also observed during the rest period. However, during the 2C charging phase, the temperature decline is less pronounced compared to the 1C charging in Type I cycles. Owing to the higher heat generation rate associated with 2C charging, $T_{Max,Sur}$ of around 317 K is maintained. This behaviour indicates a thermal balance between the heat generated and the heat dissipation within the pure PCM. Additionally, as shown in Fig. 8 (b) and the liquid

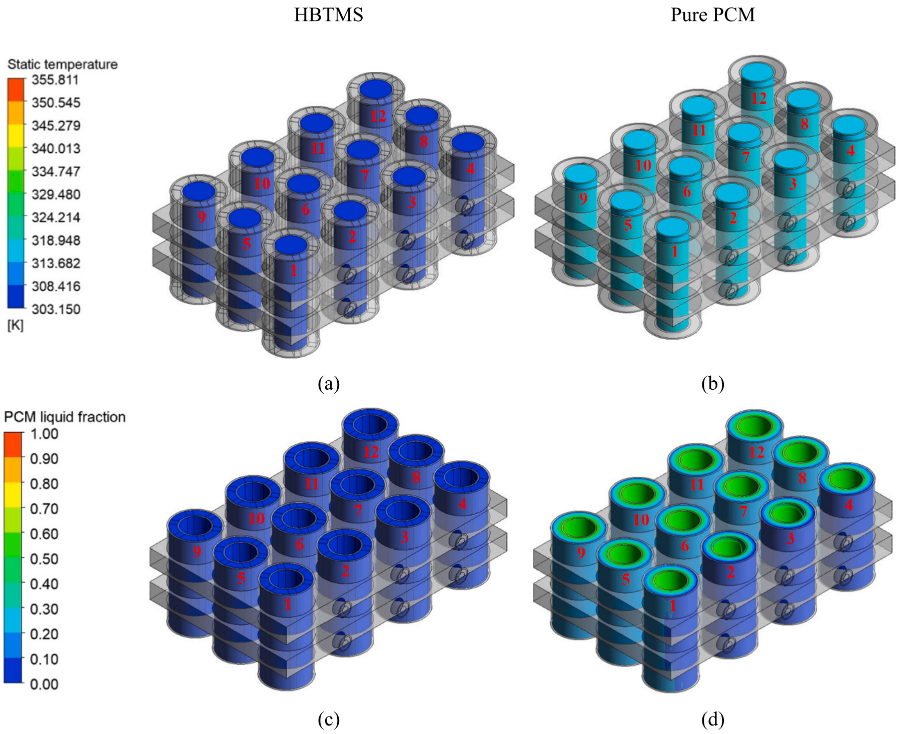

(a) (b)

(c) (d)

First Cycle

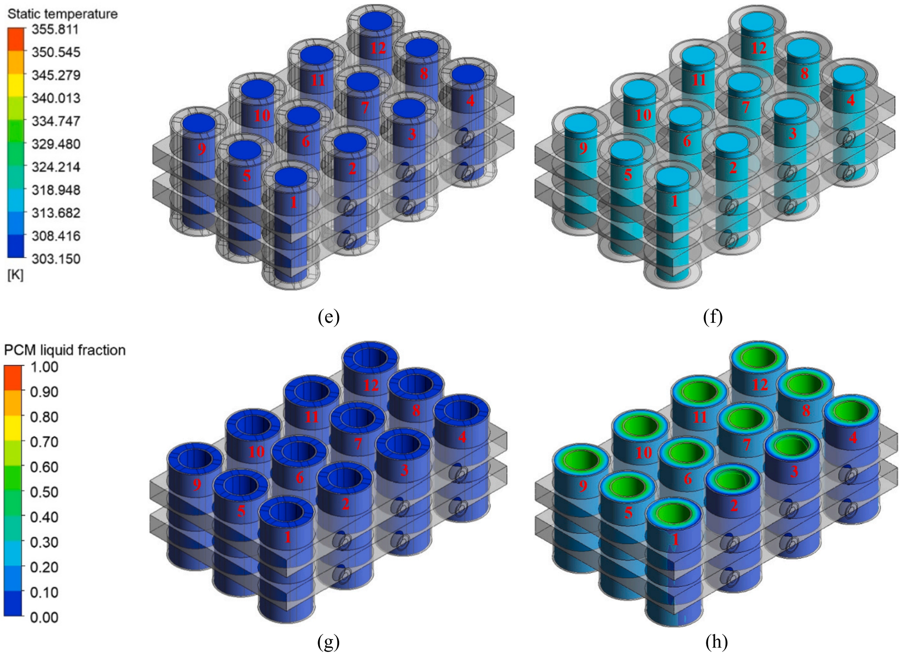

(e) (f)

(g) (h)

Fifth Cycle

Fig. 7. Static temperature and PCM liquid fraction contour plots of the HBTMS and pure PCM cooling under Type I cycles at the end of the first and fifth cycle.

fraction contour plot at the end of the first cycle in Fig. 9 (d), the PCM is not fully melted and L_f reached approximately 0.59. This represents a 90% increase compared to the maximum L_f observed under Type I cycles for pure PCM cooling, reflecting the greater thermal load in Type II cycles. For the HBTMS, a similar $T_{Max,Sur}$ of 312.215 K is observed by the end of the first discharge, which is 10.9 K below the safety limit. Notably, during both the rest and 2C charging phases, $T_{Max,Sur}$ continues to decline and even drops below the ambient temperature, despite the higher heat generation compared to the 1C charging in Type I cycles. However, a comparison of the static temperature contours in Fig. 7 (a) and Fig. 9 (a) reveals a slight increase in the battery core temperature under Type II cycles relative to Type I, attributable to the increased thermal load. Nevertheless, the HBTMS exhibits a similar PCM phase change pattern during the first Type II cycle as in Type I, with complete solidification of the PCM by the end of the cycle. This indicates full restoration of the PCM's latent heat capacity, confirming the system's capacity to manage elevated thermal loads while maintaining stable and reversible thermal behaviour.

As depicted in Fig. 8 (a), during successive Type II cycles, the $T_{Max,Sur}$ under pure PCM cooling increases rapidly, reaching values of 321.821 K,

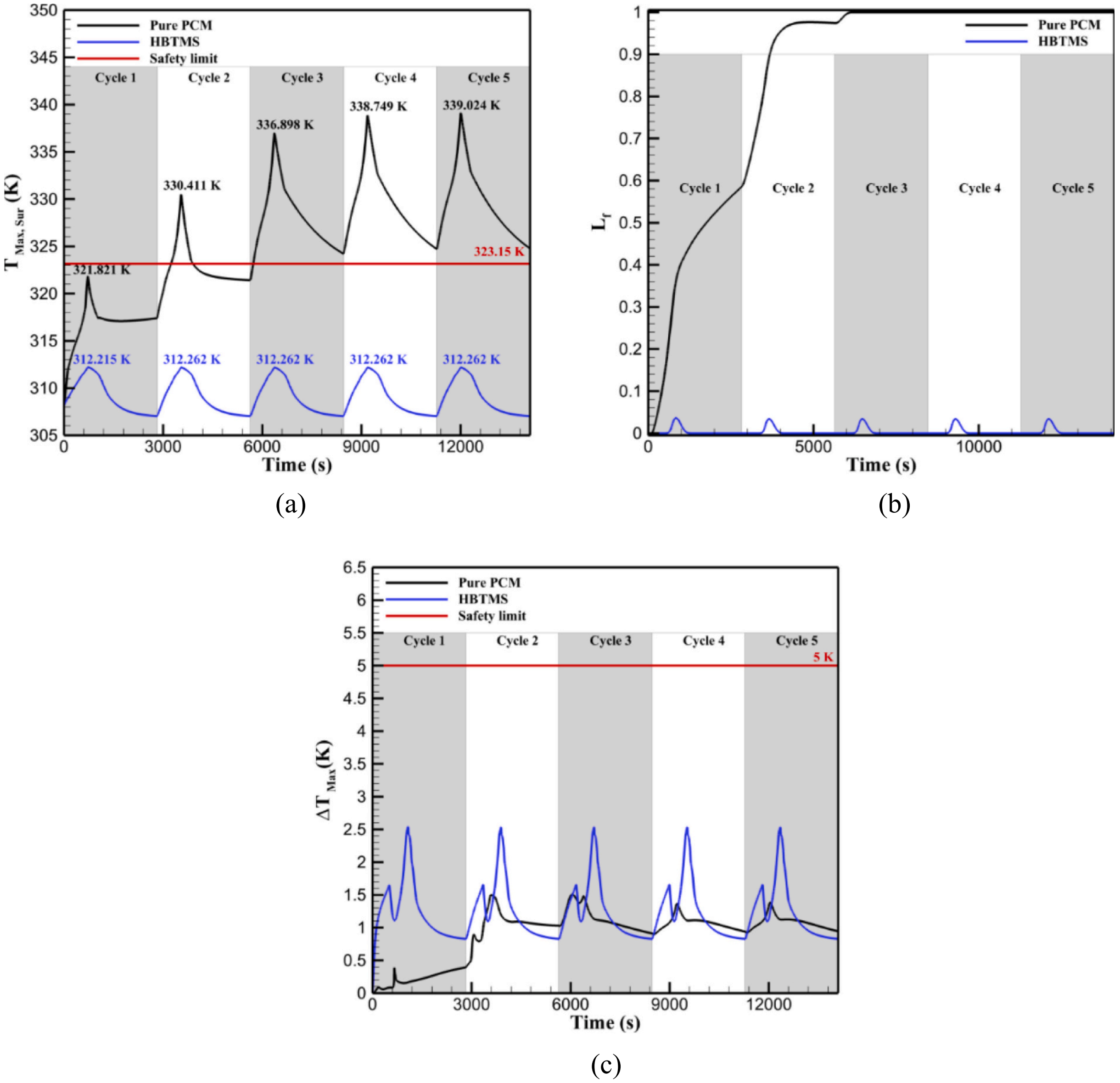

Fig. 8. Performance of the HBTMS under Type II cycles in terms of (a) maximum battery surface temperature, (b) PCM liquid fraction, and (c) maximum temperature difference within the battery module.

330.411 K, 336.898 K, 338.749 K, and 339.024 K at the end of discharge in the first through fifth cycles, respectively. Compared to the Type I cycles (Fig. 6 (a)), these values represent temperature increases of 3.394 K, 7.406 K, 8.093 K, and 7.805 K during the second to fifth cycles, respectively. Notably, the safety limit of 323.15 K is first exceeded during the discharge phase of the second cycle. Although $T_{Max,Sur}$ temporarily drops below the safety limit by the end of the second cycle, it consistently exceeds the limit in the subsequent three cycles. The enhanced heat generation during 2C discharge in Type II cycles intensifies the heat accumulation issue, making the limitations of pure PCM cooling more pronounced. As shown in Fig. 8 (b), the PCM undergoes continuous melting without a solidification stage, becoming fully saturated early in the third cycle's discharge phase, an observation supported by the liquid fraction contour plots in Fig. 9 (d) and (h). In contrast, the HBTMS maintains superior thermal stability throughout all cycles. As shown in Fig. 8 (a), the maximum $T_{Max,Sur}$ remains nearly constant, reaching 312.262 K from the second to the fifth cycle, only a minor increase of 0.04 K from the first cycle and still 10.88 K below the safety limit. Compared to Type I cycles, the maximum $T_{Max,Sur}$ increases by only 0.08 K, further underscoring that the system is significantly less sensitive to cycle type under HBTMS operation. A comparison of the static temperature contour plots by the end of the first and fifth cycles (Fig. 9 (a) and (e)) reveals that HBTMS maintains a nearly identical temperature distribution across both the battery surface and core. In contrast, for the pure PCM system, a comparison of Fig. 9 (b) and (f) highlights a substantial temperature increase by the fifth cycle, particularly at the battery core. The PCM phase change patterns further confirm these observations. As shown in Fig. 8 (b), the HBTMS supports a repeatable melting and solidification cycle, allowing full restoration of the PCM's latent heat capacity. This is evidenced by the liquid fraction contour plots, where complete solidification is evident at the end of the fifth cycle for the HBTMS (Fig. 9 (g)). Conversely, for the pure PCM system, the PCM remains fully melted at the end of the fifth cycle (Fig. 9 (h)), indicating ineffective thermal recovery.

In terms of ΔT_{Max}, Fig. 8 (c) depicts that both systems maintain ΔT_{Max} below the safety limit of 5 K under Type II cycles, despite observable fluctuations. For the pure PCM cooling system, ΔT_{Max} increases over the first three cycles, reaching a peak of approximately 1.5 K during the third cycle. After the PCM becomes fully melted, ΔT_{Max} slightly decreases to around 1.3 K. Compared to Type I cycles, greater

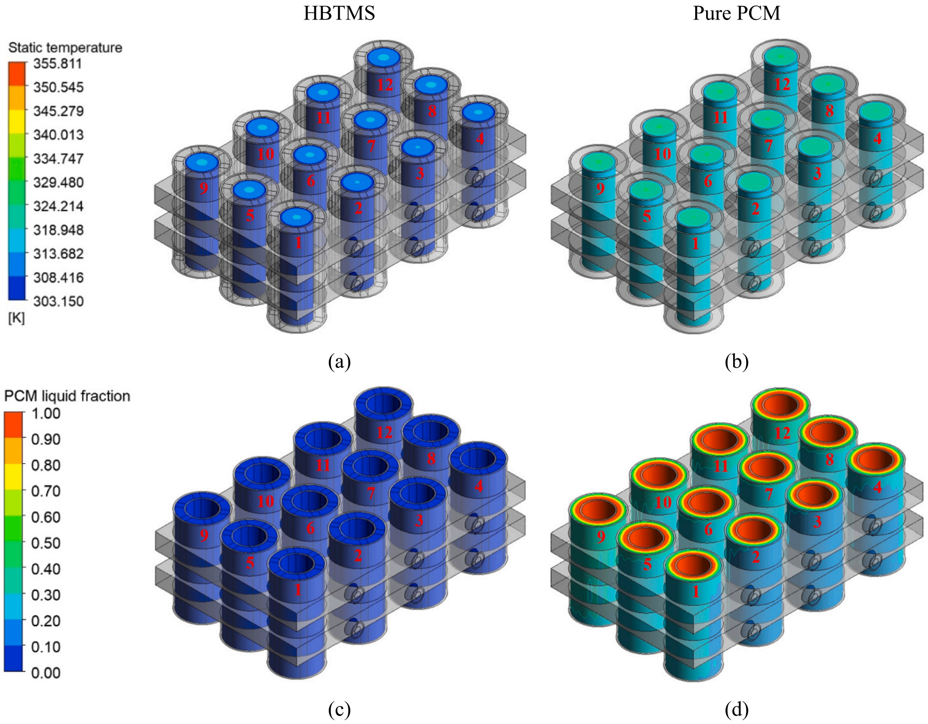

(a) (b)

(c) (d)

First Cycle

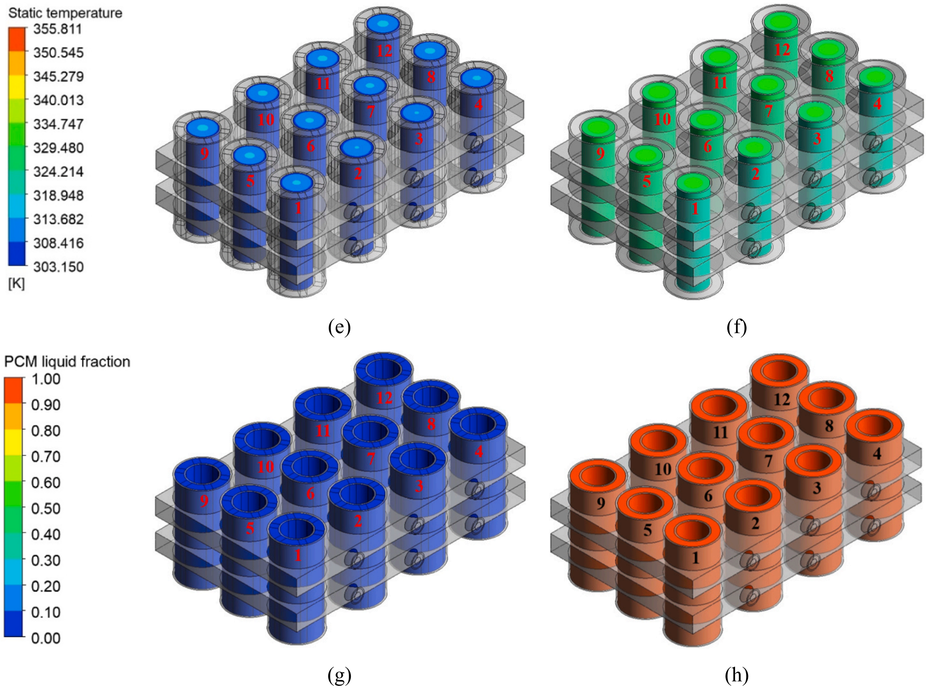

(e) (f)

(g) (h)

Fifth Cycle

Fig. 9. Static temperature and PCM liquid fraction contour plots of the HBTMS and pure PCM cooling under Type II cycles at the end of the first and fifth cycle.

thermal uniformity was observed in the pure PCM system under Type II cycles, due to increased PCM melting driven by the higher heat generation associated with 2C charging. In comparison, the HBTMS exhibits a similar trend to that observed in Type I cycles, with a slight upward shift of approximately 0.5 K. A consistent maximum ΔT_{Max} of around 2.5 K is recorded at the end of the discharge phase in each cycle. Notably, by the end of each cycle, the HBTMS demonstrates lower ΔT_{Max} values than the pure PCM system, indicating superior thermal uniformity. This performance is attributed to the higher heat generation during the 2C charging stages and the enhanced thermal regulation capabilities of the HBTMS. Moreover, while the range of ΔT_{Max} variation for the HBTMS across cycles is approximately 1.5 K, it remains significantly narrower, around 0.4 K, for the pure PCM system. This variation is likely due to the spatial differences in liquid cooling effectiveness within the HBTMS, where batteries positioned in the first row benefit more from lower inlet temperatures, particularly during the rest and charging stages.

4.2.3. Type III cycles (charging at 3C and discharging at 5C)

The performance of pure PCM cooling and the HBTMS under Type III cycles is presented in Fig. 10. As shown in Fig. 10 (a), for the pure PCM system, $T_{Max,Sur}$ reached 321.821 K at the end of the 5C discharge during the first cycle and then decreased to approximately 317 K during the subsequent rest period. However, unlike the other cycle types, the higher heat generation during the 3C charging stage causes $T_{Max,Sur}$ to rise again, approaching but remaining just below the safety threshold of 323.15 K by the end of the first cycle. Due to the significantly high heat generation during both discharge and charge phases, the PCM experiences substantial melting. As shown in Fig. 10 (b), the L_f reached a value of 0.74 by the end of the first cycle. This is further supported by the contour plot in Fig. 11 (d), which shows a considerable portion of the PCM in the melted state. In contrast, the HBTMS demonstrates a more controlled thermal response. After reaching a maximum $T_{Max,Sur}$ of 312.215 K at the end of the discharge phase, the temperature continued to decline throughout the rest and charging periods, reaching approximately 310 K by the end of the first cycle. However, this final temperature is higher than the values observed at the end of the first cycles in Type I and II, reflecting the increased thermal load in Type III cycles. As shown in Fig. 11 (a), a larger temperature gradient between the core and surface of the battery was observed by the end of the first cycle under Type III cycles. This gradient is more pronounced in the pure PCM system, as illustrated in Fig. 11 (b), due to its limited thermal conductivity and inability to effectively manage the intensified heat generation. Nevertheless, the HBTMS continues to support stable thermal behaviour. As with the previous cycle types, the PCM undergoes melting during discharge and is fully solidified by the end of the cycle, thereby restoring its latent heat capacity and ensuring consistent thermal performance.

During subsequent cycles, the pure PCM cooling system, as illustrated in Fig. 10 (a), exhibited increasingly unfavourable thermal performance. The system exceeded the safety threshold of 323.15 K from the second to fifth cycles, with maximum $T_{Max,Sur}$ recorded at 321.821 K, 333.956 K, 344.566 K, 347.143 K, and 347.742 K during the first to fifth cycles, respectively. These values represent increases of 6.939 K, 15.074 K, 16.487 K, and 16.523 K compared to the corresponding maximum temperatures under Type I cycles, indicating significant heat

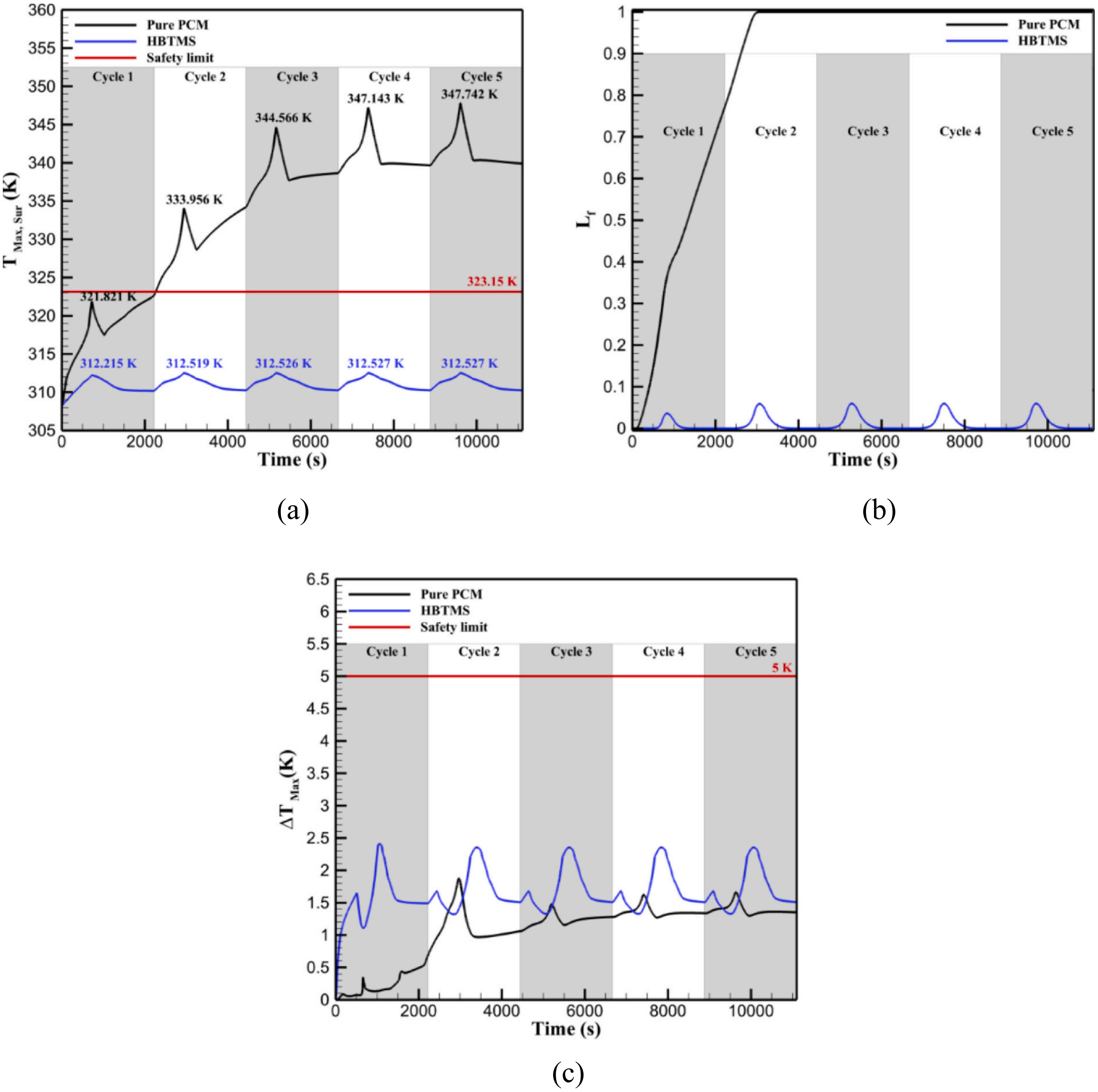

(a)

(b)

(c)

Fig. 10. Performance of the HBTMS under Type III cycles in terms of (a) maximum battery surface temperature, (b) PCM liquid fraction, and (c) maximum temperature difference within the battery module.

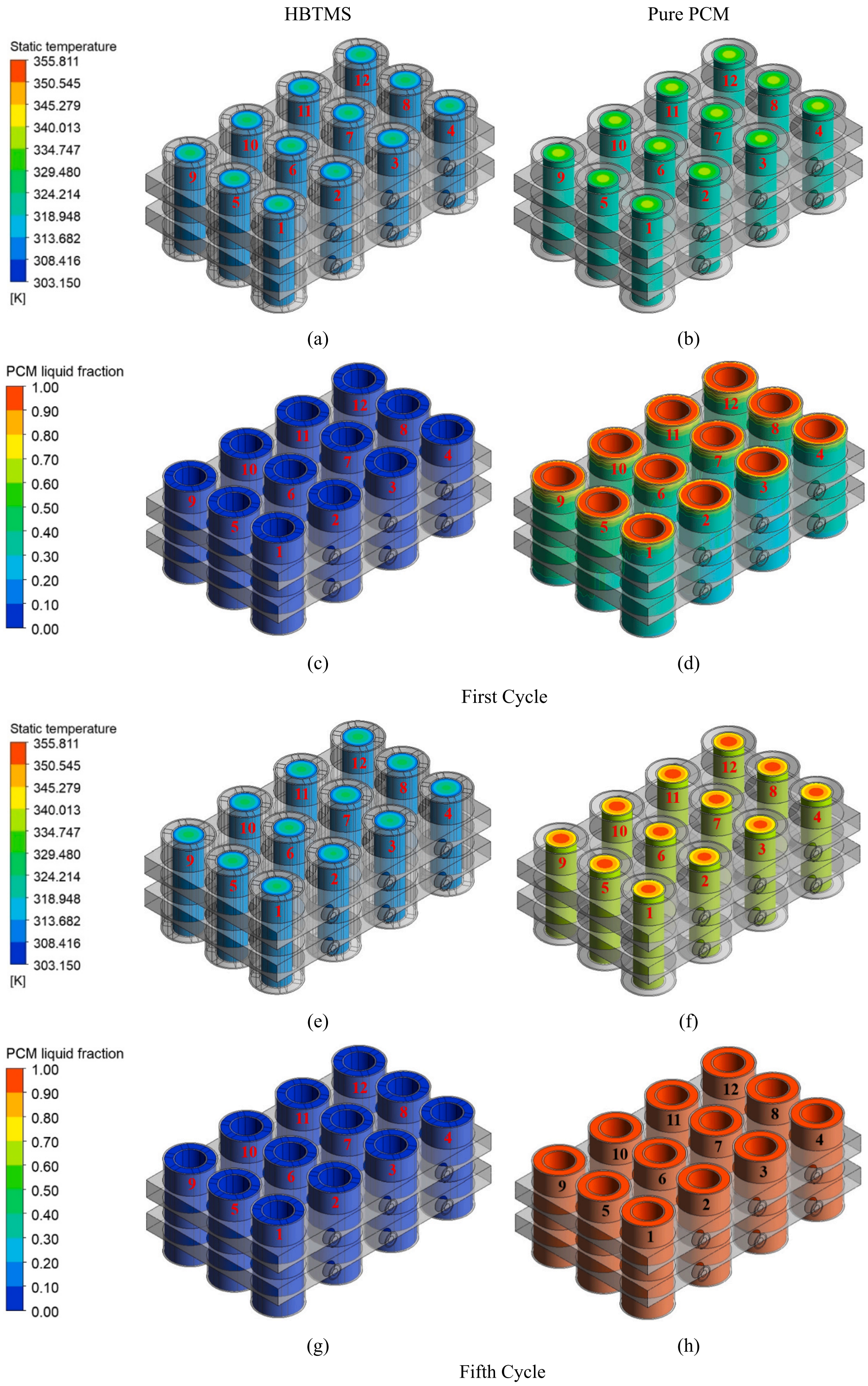

(a) (b)

(c) (d)

First Cycle

(e) (f)

(g) (h)

Fifth Cycle

Fig. 11. Static temperature and PCM liquid fraction contour plots of the HBTMS and pure PCM cooling under Type III cycles at the end of the first and fifth cycle.

accumulation over time. As shown in Fig. 10 (b), the pure PCM system undergoes rapid PCM melting, with full melting occurring as early as the second cycle. This is further supported by Fig. 11 (h), which reveals that the PCM does not solidify in the subsequent cycles. This behaviour is primarily attributed to the limited heat transfer in the pure PCM cooling and the elevated heat generation associated with 5C discharge and 3C charge. Consequently, the system fails to dissipate heat effectively, leading to sustained PCM thermal saturation and severe temperature rise. Additionally, the difference in $T_{Max,Sur}$ between cycles becomes less pronounced after PCM saturation, particularly in the fourth and fifth cycles. In contrast, the HBTMS consistently maintains stable thermal performance, as in previous cycle types. The maximum $T_{Max,Sur}$ is limited to approximately 312.526 K, representing only a marginal increase of 0.34 K compared to Type I cycles, and remains 10.62 K below the safety limit. The static temperature contour plots in Fig. 11 (a) and (e) reveal that the temperature gradient between the battery surface and core remains nearly unchanged between the first and fifth cycles, confirming the consistent thermal regulation offered by the HBTMS. By comparison, under pure PCM cooling, the core temperature increases significantly and reaches 355.811 K by the end of the fifth cycle, as evident in Fig. 11 (f). This further demonstrates the thermal instability and poor heat dissipation of the pure PCM system under high thermal loads. As shown in Fig. 10 (b) and the liquid fraction contour plots (Fig. 11 (c) and (g)), the HBTMS continues to support PCM melting during discharge and complete solidification by the end of each cycle. This enables full restoration of the latent heat capacity and ensures effective thermal cycling and long-term durability.

In terms of the ΔT_{Max}, both systems maintained values below the safety limit of 5 K under Type III cycles, as illustrated in Fig. 10 (c). For the pure PCM cooling ΔT_{Max} increased to approximately 1.8 K during the second cycle, coinciding with the complete melting of the PCM. In the subsequent three cycles, ΔT_{Max} slightly decreased and stabilised at around 1.5 K, likely due to the fully melted state of the PCM and the reduced thermal gradients resulting from saturation. The HBTMS exhibited a similar performance trend to that observed in Type II cycles, with maximum ΔT_{Max} of approximately 2.5 K across the different cycles, an increase of about 0.5 K compared to Type I cycles. These values fluctuated in the range of 1.2 to 2.5 K, influenced by the cyclic melting and solidification of the PCM as well as the variable heat generation during different phases of each cycle. In contrast to the earlier cycle types, the HBTMS showed a slightly higher ΔT_{Max} of around 0.25 K at the end of each cycle compared to the pure PCM system. This is likely due to the increased thermal load in Type III cycles and the resulting temperature gradients within the hybrid system, despite its superior overall cooling performance and thermal stability.

It is important to distinguish between short-term thermal buffering and long-term cyclic sustainability. A configuration may successfully limit maximum temperature during a single discharge; however, if latent heat recovery during the rest and charge phase is incomplete, thermal performance will progressively degrade. The stable cyclic behaviour observed here demonstrates that the proposed HBTMS maintains a dynamic balance between heat absorption and regeneration, ensuring sustained thermal control over repeated cycling.

From a physical standpoint, cyclic performance is governed by three interacting mechanisms: (i) the rate of latent heat absorption during discharge, (ii) the effectiveness of PCM re-solidification during rest and charging, and (iii) the balance between cumulative heat removal by the coolant and residual heat accumulation within the module. The long-term stability of the HBTMS therefore depends not only on maximum temperature control, but also on the ability of the system to fully regenerate its latent heat capacity between successive cycles.

In the context of EV applications, the temperature non-uniformity metric (ΔT_{Max}) is particularly important, as it governs cell-to-cell performance dispersion, imbalance growth, and divergence in ageing rates across a module. Elevated and spatially non-uniform temperatures accelerate capacity fade, impedance growth, and lithium plating risk, thereby shortening effective pack lifetime and increasing the balancing burden on the battery management system. The present results demonstrate that the proposed HBTMS maintains ΔT_{Max} below the commonly accepted 5 K uniformity threshold under repeated high-rate cycling, indicating its capability to limit thermally induced mismatch and associated degradation pathways. From a vehicle integration perspective, the boundary conditions applied in this study, namely coolant inlet temperature, mass flow rate, and ambient temperature, directly correspond to the constraints imposed by an EV low-temperature thermal loop and surrounding environment. Consequently, the reported trends are transferable to module-level systems, provided that equivalent inlet conditions and coolant distribution uniformity are maintained across parallel flow paths.

It should be noted that the five-cycle analysis presented here is illustrative rather than lifetime-representative. The selected discharge and charge rates represent severe operating conditions intended to approximate high-power, worst-case EV scenarios in terms of aggressive acceleration, fast charging, or elevated ambient conditions, thereby providing a conservative assessment of thermal robustness. The absence of progressive temperature escalation and the effective restoration of latent heat capacity between cycles indicate that the proposed HBTMS can sustain thermal margins under repeated high-load events. While extended ageing studies would be required to quantify long-term degradation effects, the demonstrated cyclic stability suggests that the combined convective heat extraction and PCM buffering mechanisms are compatible with realistic EV operating envelopes and supportive of improved module-level longevity.

5. Conclusion

Multi-objective optimisation using the “mean of means” method identified the optimal design configuration as comprising two cooling plates, an ambient temperature of 308.15 K, a coolant temperature of 298.15 K, and a coolant flow rate of 0.001 kg/s. In terms of porous media, a fin thickness of 4 mm, six fins with porosity of 0.8 and 20 PPI pore density, and a porous layer with 4 mm thickness, 0.8 porosity, and 20 PPI were found to yield the best overall system performance. This combination achieved a favourable balance between thermal regulation by minimising $T_{Max,\ Sur}$ and ΔT_{Max} and structural efficiency by maximising both PEC and E_d. Cyclic performance evaluation demonstrated that the proposed HBTMS significantly outperforms pure PCM cooling under repeated high-rate discharge–rest–charge cycles. Across all three tested scenarios i.e. Type I, II and III (with fixed 5C discharge and 1C—3C charging rates), the HBTMS consistently maintained $T_{Max,\ Sur}$ at approximately 312–312.5 K, remaining at least 10 K below the safety limit of 323.15 K. In contrast, the pure PCM system exhibited progressive thermal degradation, $T_{Max,\ Sur}$ exceeding the safety threshold from the second cycle onwards and reaching up to 347.7 K under Type III cycles. The HBTMS also ensured full PCM solidification at the end of each cycle, supporting repeatable phase change behaviour and complete latent heat recovery. By comparison, the pure PCM system showed increasing liquid fraction across cycles, indicating incomplete solidification, heat accumulation, and loss of cooling capacity. In terms of temperature uniformity, the HBTMS maintained ΔT_{Max} within 2–2.5 K across all cycles, with minimal variation, while the pure PCM system experienced greater fluctuation due to PCM saturation. Even under the most demanding Type III cycles, the HBTMS upheld thermal stability and durability, confirming its suitability for long-term battery operation under cyclic high-load conditions.

Although the present study demonstrates robust thermal performance, certain modelling simplifications represent limitations that warrant further investigation. Future work could extend the present modelling framework to enable a more detailed and realistic assessment of the proposed HBTMS under high-rate and long-term operating conditions. In particular, the incorporation of temperature-dependent thermophysical properties for the PCM and coolant, consideration of volumetric changes during PCM phase transition, and the adoption of more advanced battery heat generation models could be investigated. Furthermore, large-scale pack integration will require careful evaluation of coolant distribution uniformity and manifold design, which were not explicitly addressed in the present cell-level model. Such investigations will enable evaluation of fabrication feasibility, interfacial thermal behaviour, coolant-side fouling and clogging risk within porous inserts, long-term mechanical durability under cyclic loading, and cost–performance trade-offs. These developments would provide deeper insight into the practical applicability, reliability, and robustness of the proposed HBTMS for sustained cyclic operation in real-world scenarios.

CRediT authorship contribution statement

Alireza Keyhani-Asl: Writing – review & editing, Writing – original draft, Visualization, Validation, Software, Methodology, Investigation, Formal analysis. **Noel Perera:** Writing – review & editing, Supervision, Project administration. **Jens Lahr:** Supervision. **Reaz Hasan:** Writing –

review & editing, Supervision, Conceptualization. **Parvaneh Zare:** Writing – review & editing, Software, Methodology.

Funding

This research did not receive any specific grant from funding agencies in the public, commercial, or not-for-profit sectors.

Declaration of competing interest

The authors declare that they have no known competing financial interests or personal relationships that could have appeared to influence the work reported in this paper.

Acknowledgments

The authors gratefully acknowledge Dr. Roger Tait for his expert guidance and insightful advice regarding the utilisation of the HPC (Cluster 3) resource. Appreciation is also extended to the Department of Engineering, School of Architecture, Built Environment, Computing and Engineering at Birmingham City University for their support in enabling access to this computational facility.

Data availability

Data will be made available on request.

References

[1] A. Angani, H.-W. Kim, M.-H. Hwang, E. Kim, K.-M. Kim, H.-R. Cha, A comparison between Zig-Zag plated hybrid parallel pipe and liquid cooling battery thermal management systems for Lithium-ion battery module, Appl. Therm. Eng. 219 (2023) 119599.
[2] P.G. Zadeh, Y. Wang, J.D. Chung, Thermal management modeling for cylindrical lithium-ion battery packs considering safety and lifespan, J. Mech. Sci. Technol. 36 (7) (2022) 3727–3733.
[3] P. Zare, N. Perera, J. Lahr, R. Hasan, A novel thermal management system for cylindrical lithium-ion batteries using internal-external fin-enhanced phase change material, Appl. Therm. Eng. 238 (2024) 121985.
[4] W. Wu, S. Wang, W. Wu, K. Chen, S. Hong, Y. Lai, A critical review of battery thermal performance and liquid based battery thermal management, Energy Convers. Manag. 182 (2019) 262–281.
[5] P. Zare, N. Perera, J. Lahr, R. Hasan, Solid-liquid phase change materials for the battery thermal management systems in electric vehicles and hybrid electric vehicles–a systematic review, J. Energy Storage 52 (2022) 105026.
[6] A. Keyhani-Asl, N. Perera, J. Lahr, R. Hasan, Porous media and foam application in battery thermal management systems: a comprehensive review focused on its impact, numerical modeling, and experimental preparation, J. Energy Storage 93 (2024) 112306.
[7] P. Zare, N. Perera, J. Lahr, R. Hasan, Uniform temperature distribution, prolonged temperature regulation, and accelerated recovery of battery thermal management system using a novel fin design, J. Energy Storage 108 (2025) 115054.
[8] J.R. Patel, M.K. Rathod, Recent developments in the passive and hybrid thermal management techniques of lithium-ion batteries, J. Power Sources 480 (2020) 228820.
[9] M. Waseem, M. Ahmad, A. Parveen, M. Suhaib, Battery technologies and functionality of battery management system for EVs: current status, key challenges, and future prospectives, J. Power Sources 580 (2023) 233349.
[10] H.N. Khaboshan, K. Kadirgama, D. Ramasamy, V. Talele, P. Zhao, H. Tyagi, N. Miljkovic, Thermal uniformity analysis of a hybrid battery pack using integrated phase change material, metal foam, and counterflow minichannels, Appl. Therm. Eng. 259 (2025) 124910.
[11] A. Moaveni, M. Siavashi, S. Mousavi, Passive and hybrid battery thermal management system by cooling flow control, employing nano-PCM, fins, and metal foam, Energy 288 (2024) 129809.
[12] Y. Zhao, B. Zou, J. Ding, Y. Ding, Experimental and numerical investigation of a hybrid battery thermal management system based on copper foam-paraffin composite phase change material and liquid cooling, Appl. Therm. Eng. 218 (2023) 119312.
[13] H. Xie, H. Chen, C. Shi, C. Liu, M. Li, W. Chang, A hybrid battery thermal management system coupling liquid immersion cooling with phase change material for HEVs, Appl. Therm. Eng. 292 (2026) 130325.
[14] J. Li, J. Yang, Y. Sun, X. Ren, Performance analysis of battery thermal management system composed of copper foam/paraffin and wavy liquid cooling microchannels, Renew. Energy 256 (2026) 123928.
[15] V.A. Wagh, S.K. Saha, On estimating critical channel number of hybrid battery thermal management system combining phase change material and forced convective immersion cooling, Int. Commun. Heat Mass Transfer 171 (2026) 110114.
[16] H. Liu, S. Ahmad, Y. Shi, J. Zhao, A parametric study of a hybrid battery thermal management system that couples PCM/copper foam composite with helical liquid channel cooling, Energy 231 (2021) 120869.
[17] M.M. El Idi, M. Karkri, M.A. Tankari, A passive thermal management system of Li-ion batteries using PCM composites: experimental and numerical investigations, Int. J. Heat Mass Transf. 169 (2021) 120894.
[18] J. Lin, D. Liu, X. Liu, M. Liu, Y. Cui, CNT@ MXene porous composite PCM based thermal management for lithium-ion battery system, Appl. Therm. Eng. 262 (2025) 125240.
[19] Z. Liu, S. Ji, B. Wang, P. Li, Lightweight lithium-ion battery hybrid cooling system and intermittent cycle operation strategy design under demanding conditions, Int. Commun. Heat Mass Transfer 160 (2025) 108304.
[20] V. Saxena, S.K. Sahu, S.I. Kundalwal, P.A. Tsai, Enhanced thermal management system for Li-ion batteries using phase change material and liquid cooling under realistic driving cycles, Energy 318 (2025) 134759.
[21] Z. Liu, B. Wang, Y. Tan, P. Li, Thermal management of lithium-ion battery pack under demanding conditions and long operating cycles using fin-enhanced PCMs/water hybrid cooling system, Appl. Therm. Eng. 233 (2023) 121214.
[22] J. Wang, W. Mei, B. Mao, Q. Wang, Investigation on the temperature control performance and optimization strategy of a battery thermal management system combining phase change and liquid cooling, Appl. Therm. Eng. 232 (2023) 121080.
[23] H. Huang, H. Wang, J. Gu, Y. Wu, High-dimensional model representation-based global sensitivity analysis and the design of a novel thermal management system for lithium-ion batteries, Energy Convers. Manag. 190 (2019) 54–72.
[24] Z. Sun, Y. Guo, C. Zhang, J. Whitehouse, Q. Zhou, H. Xu, C. Wang, Experimental study of battery passive thermal management system using copper foam-based phase change materials, Int. J. Thermofluids 17 (2023) 100255.
[25] B. Li, L. Zhang, B. Shang, Y. Huo, Numerical investigation on heat transfer characteristics in battery thermal management with phase change material composited by toroidal porous medium, Int. Commun. Heat Mass Transfer 154 (2024) 107414.
[26] M. Habibishandiz, M. Saghir, A critical review of heat transfer enhancement methods in the presence of porous media, nanofluids, and microorganisms, Therm. Sci. Eng. Prog. 30 (2022) 101267.
[27] C.-T. Hsu, P. Cheng, Thermal dispersion in a porous medium, Int. J. Heat Mass Transf. 33 (8) (1990) 1587–1597.
[28] K. Vafai, Handbook of Porous Media, CRC Press, 2015.
[29] D.A. Nield, A. Bejan, Convection in porous media 3, Springer, 2006.
[30] A. Keyhani-Asl, N. Perera, J. Lahr, R. Hasan, Innovative hybrid battery thermal management system incorporating copper foam porous fins and layers with phase change material and liquid cooling, Appl. Therm. Eng. 268 (2025) 125848.
[31] A. Keyhani-Asl, N. Perera, J. Lahr, R. Hasan, Numerical analysis of copper foam-enhanced hybrid battery thermal management systems for lithium-ion batteries: advancing energy density and thermal control, Appl. Therm. Eng. 278 (2025) 127183.
[32] Y. Miao, P. Hynan, A. Von Jouanne, A. Yokochi, Current Li-ion battery technologies in electric vehicles and opportunities for advancements, Energies 12 (6) (2019) 1074.
[33] E. Jiaqiang, M. Yue, J. Chen, H. Zhu, Y. Deng, Y. Zhu, F. Zhang, M. Wen, B. Zhang, S. Kang, Effects of the different air cooling strategies on cooling performance of a lithium-ion battery module with baffle, Appl. Therm. Eng. 144 (2018) 231–241.
[34] F. Zhang, F. Lu, B. Liang, Y. Zhu, H. Gou, K. Xiao, Y. He, Thermal performance analysis of a new type of branch-fin enhanced battery thermal management PCM module, Renew. Energy 206 (2023) 1049–1063.
[35] M.M. Heyhat, S. Mousavi, M. Siavashi, Battery thermal management with thermal energy storage composites of PCM, metal foam, fin and nanoparticle, J. Energy Storage 28 (2020) 101235.
[36] S. Ambekar, P. Rath, A. Bhattacharya, A novel PCM and TCE based thermal management of battery module, Therm. Sci. Eng. Prog. 29 (2022) 101196.
[37] H. Zhang, H.W. Mu, Y. Zhang, J. Han, Calculation and characteristics analysis of lithium ion batteries' internal resistance using HPPC test, Adv. Mater. Res. 926 (2014) 915–918.
[38] S. Xin, C. Wang, H. Xi, Thermal management scheme and optimization of cylindrical lithium-ion battery pack based on air cooling and liquid cooling, Appl. Therm. Eng. 224 (2023) 120100.
[39] Y. Lai, W. Wu, K. Chen, S. Wang, C. Xin, A compact and lightweight liquid-cooled thermal management solution for cylindrical lithium-ion power battery pack, Int. J. Heat Mass Transf. 144 (2019) 118581.
[40] V.R. Voller, C. Prakash, A fixed grid numerical modelling methodology for convection-diffusion mushy region phase-change problems, Int. J. Heat Mass Transf. 30 (8) (1987) 1709–1719.
[41] M. Fadl, P.C. Eames, Numerical investigation of the influence of mushy zone parameter Amush on heat transfer characteristics in vertically and horizontally oriented thermal energy storage systems, Appl. Therm. Eng. 151 (2019) 90–99.
[42] M. Bamdezh, G. Molaeimanesh, S. Zanganeh, Role of foam anisotropy used in the phase-change composite material for the hybrid thermal management system of lithium-ion battery, J. Energy Storage 32 (2020) 101778.
[43] P.J. Roache, Perspective: a method for uniform reporting of grid refinement studies, J. Fluid Eng. 116 (3) (1994) 405–413.
[44] Division, A.S.o.M.E.F.E, Quantification of Uncertainty in Computational Fluid Dynamics, American Society of Mechanical Engineers, 1993.
[45] R. Oliveira, G. Justi, G. Lopes, Grid convergence study of a cyclone separator using different mesh structures, Chem. Ind. Chem. Eng. Q. 23 (3) (2017) 311–320.

[46] S. Sudhakaran, M. Terese, Y. Mohan, A.D. Thampi, S. Rani, Influence of various parameters on the cooling performance of battery thermal management systems based on phase change materials, Appl. Therm. Eng. 222 (2023) 119936.
[47] A. Bademlioglu, A. Canbolat, N. Yamankaradeniz, O. Kaynakli, Investigation of parameters affecting organic Rankine cycle efficiency by using Taguchi and ANOVA methods, Appl. Therm. Eng. 145 (2018) 221–228.
[48] S.K. Saha, H. Ranjan, M.S. Emani, A.K. Bharti, Performance Evaluation Criteria in Heat Transfer Enhancement, Springer, 2020.
[49] J. Zhang, X. Li, G. Zhang, H. Wu, Z. Rao, J. Guo, D. Zhou, Experimental investigation of the flame retardant and form-stable composite phase change materials for a power battery thermal management system, J. Power Sources 480 (2020) 229116.
[50] Minitab, Methods and Formulas for Analyze Taguchi Design, Available from: https://support.minitab.com/en-us/minitab/help-and-how-to/statistical-modeling/doe/how-to/taguchi/analyze-taguchi-design/methods-and-formulas/methods-and-formulas/, 2024.
[51] M.S. Phadke, Quality Engineering Using Robust Design, Prentice Hall PTR, 1995.
[52] M.R. Giuliano, A.K. Prasad, S.G. Advani, Experimental study of an air-cooled thermal management system for high capacity lithium–titanate batteries, J. Power Sources 216 (2012) 345–352.
[53] X. Hu, F. Zhu, X. Gong, Experimental and numerical study on the thermal behavior of phase change material infiltrated in low porosity metal foam, J. Energy Storage 26 (2019) 101005.
[54] M. Amani, M. Ameri, A. Kasaeian, The experimental study of convection heat transfer characteristics and pressure drop of magnetite nanofluid in a porous metal foam tube, Transp. Porous Media 116 (2017) 959–974.
[55] J.R. Patel, M.K. Rathod, Phase change material selection using simulation-oriented optimization to improve the thermal performance of lithium-ion battery, J. Energy Storage 49 (2022) 103974.